Disequilibrium Dihedral Angles in Layered Intrusions: a Microstructural Record of Fractionation

MARIAN B. HOLNESS[1]*, OLIVIER NAMUR[1,2] AND R. GRANT CAWTHORN[3]

[1]DEPARTMENT OF EARTH SCIENCES, UNIVERSITY OF CAMBRIDGE, DOWNING STREET, CAMBRIDGE CB2 3EQ, UK

[2]INSTITUT FÜR MINERALOGIE, LEIBNIZ UNIVERSITÄT, CALLINSTR. 3, D-30167 HANNOVER

[3]DEPARTMENT OF GEOLOGY AND GEOPHYSICS, UNIVERSITY OF THE WITWATERSRAND, PRIVATE BAG 3, PO WITS 2050, JOHANNESBURG, SOUTH AFRICA

The dihedral angle formed at junctions between two plagioclase grains and a grain of augite is only very rarely in textural equilibrium in gabbros from kilometre-scale crustal layered intrusions. The median of a population of these disequilibrium angles, Θ_{cpp}, varies systematically within a single layered intrusion, remaining constant over large stretches of stratigraphy with significant increases and decreases associated with the addition or reduction respectively of the number of phases on the liquidus of the bulk magma. The stepwise changes in Θ_{cpp} are present in the Upper Zone of the Bushveld Complex, the Megacyclic Unit I of the Sept Iles Intrusion, and the Layered Series of the Skaergaard intrusion. The plagioclase-bearing cumulates of Rum have a bimodal distribution of Θ_{cpp}, dependent on whether the cumulus assemblage includes clinopyroxene. The presence of the stepwise changes is independent of the order of arrival of cumulus phases and of the composition of either the cumulus phases or the inferred composition of the interstitial liquid. The only parameter that behaves in an exactly analogous manner to Θ_{cpp} is the rate of change in enthalpy with temperature ($\Delta H/\Delta T$) during crystallization. Both $\Delta H/\Delta T$ and Θ_{cpp} increase with the addition of a liquidus phase, and decrease with the removal of a liquidus phase. The replacement of one phase by another has little effect on $\Delta H/\Delta T$ and no discernible effect on Θ_{cpp}. An increase of $\Delta H/\Delta T$ results in an increase in the fraction of the total enthalpy budget that is the latent heat of crystallization (the fractional latent heat). It also increases the mass crystallized in each incremental temperature drop (the crystal productivity). These increases of both fractional latent heat and crystal productivity are likely to cause an increase in the time taken to form three-grain junctions in the mush via thermal buffering of a thickened mushy layer. We suggest these are the underlying causes of stepwise increases in Θ_{cpp}. Stepwise changes in the geometry of three-grain junctions in fully solidified gabbros thus provide a clear microstructural marker for the progress of fractionation down the liquid line of descent in layered intrusions.

INTRODUCTION

Despite decades of work by many distinguished scientists, our understanding of the way mafic layered intrusions solidify is fraught with controversy. There is considerable dispute over the fluid dynamics acting in large magma bodies (Marsh, 1989, 1991; Huppert & Turner, 1991). The mechanism by which the bulk magma is fractionated is unknown (see Morse, 1986; Tait & Jaupart, 1992; McKenzie, 2011). It has even been questioned whether fractionation in the observable magma chamber occurs at all (e.g. Marsh, 2006; although see Latypov, 2009). What is missing from these debates is a firm picture of the crystal mush layers that develop on the margins of large magma chambers. Direct observation and sampling of actively crystallizing lava lakes has given us an excellent view of what occurs

*Corresponding author. E-mail: marian@esc.cam.ac.uk.

during the solidification of 100 m-scale bodies (Helz, 1987) but we do not have comparable information about kilometre-scale intrusions. Much of what we know is derived from geochemical studies of fully solidified bodies, together with inferences from theoretical models (e.g. McKenzie, 2011). However, recent work has suggested that valuable, and hitherto unavailable, information can be obtained from a detailed study of the geometry of three-grain junctions in fully solidified gabbros and dolerites (Holness et al., 2012a).

The median clinopyroxene–plagioclase–plagioclase dihedral angle, or Θ_{cpp}, is generally out of textural equilibrium and varies systematically within and between intrusions (Holness, 2010). It has been suggested that these changes reflect differences in cooling history, caused by changes in the relative rates of growth of plagioclase and augite in the immediate vicinity of the nascent three-grain junction (Holness et al., 2012a, 2012b). In this contribution we show that the spatial variation of Θ_{cpp} is a sensitive indicator of fractionation, with significantly different behaviour in dolerites (which can be thought of as essentially unfractionated) compared with layered intrusions (formed from effectively fractionating liquids). We argue that these differences reflect fundamental differences in the thermal regimes experienced by crystal mush layers in unfractionated and fractionated solidifying mafic magma bodies. Our work paves the way towards a quantitative model of crystallization in layered intrusions, based on straightforward microstructural observations of fully solidified cumulates.

PREVIOUS WORK

Earlier studies on the variation of disequilibrium dihedral angles in layered intrusions were concentrated on the Rum and Skaergaard intrusions. It was shown that the first-order control on Θ_{cpp} in plagioclase-rich cumulates of the Eastern Layered Series of the Rum Igneous Complex is whether or not clinopyroxene is part of the liquidus assemblage. Troctolitic cumulates (olivine and plagioclase as cumulus phases with interstitial clinopyroxene) generally have Θ_{cpp} of ~80°, but olivine gabbroic cumulates (with augite as an additional cumulus phase) have Θ_{cpp} ~90° (Holness, 2007; Holness et al., 2007a). The Rum magma chamber was an open system, repeatedly replenished after eruption, and there are no unambiguous instances of troctolite stratigraphically overlain by gabbro that is related by continuous fractionation of a single magma batch. The bimodal variation of Θ_{cpp} thus cannot be directly and unequivocally linked to fractionation. This is, however, possible for the Skaergaard intrusion, which represents the solidified remains of a closed fractionating magma body (Wager & Deer, 1939). Θ_{cpp} in the Skaergaard floor cumulates varies in a stepwise fashion, increasing each time a new phase is added to the liquidus assemblage (Holness et al., 2007a, 2007b).

The stepwise increases observed in the Skaergaard cumulates, and the bimodal variation of Θ_{cpp} in the Rum cumulates, have been attributed to a decrease in the sub-solidus cooling rate consequent to an increase in the fractional latent heat associated with a change in the number of crystallizing phases (Holness et al., 2007b, 2009; Morse, 2011), although this suggestion has met with opposition (McBirney et al., 2009). McBirney et al. (2009), focusing only on the stratigraphically lowermost augite-in step in the Skaergaard cumulates, suggested that it is a consequence of metasomatism, although they offered neither suggestions for the process and driving force for the change in three-grain geometry, nor details of the source and composition of the fluids responsible.

Previous studies were based on the assumption, following Holness et al. (2005), that solidification creates an initial geometry of pyroxene–plagioclase–plagioclase junctions typified by a median dihedral angle of 60° and a standard deviation of 25–35°. It was suggested that this initial geometry, thought to be common to all solidified mafic bodies, was modified to variable extents in the sub-solidus, governed by the cooling rate of the fully solidified cumulate or gabbro. It has subsequently been shown that the geometry of pyroxene–plagioclase–plagioclase junctions in most kilometre-scale crustal layered intrusions is actually created during solidification, with only limited subsequent modification in the sub-solidus (Holness et al., 2012a).

Plagioclase grows early during solidification of basaltic liquids, forming a framework of tabular grains (Philpotts et al., 1998, 1999). The subsequent (and thereafter simultaneous) nucleation and growth of pyroxene first fills the wider pores and then gradually fills the narrower pores in this framework (Holness et al., 2012a). In dolerites and basalts (i.e. in closed systems with no loss of evolved interstitial liquid), pyroxene may not completely fill the narrowest pores: these become preferentially filled with silica-rich glass, granophyric intergrowths or other late-stage minerals. Microstructures in the most rapidly cooled bodies of magma are consistent with a relatively slow rate of growth of plagioclase, so the infilling pyroxene generally inherits the shape of the original melt-filled pores (Fig. 1a and b): the dihedral angle population is thus controlled by the angle at which the framework-forming plagioclase grains impinge. The resultant Θ_{cpp} does not have the expected value of 60°, however, because pyroxene does not grow into all the narrow pores. Instead, it is usually ~78° in rocks that took less than about a decade to solidify (Holness et al., 2012a, 2012b). As the cooling rate decreases, the balance between the growth rates of pyroxene and plagioclase changes. The infilling of melt-filled pores in the framework in slower-cooled rocks is achieved by coupled growth of pyroxene and the plagioclase walls. This results in a higher Θ_{cpp} (Fig. 1c and d). Although many detailed studies of the effects of cooling rate on
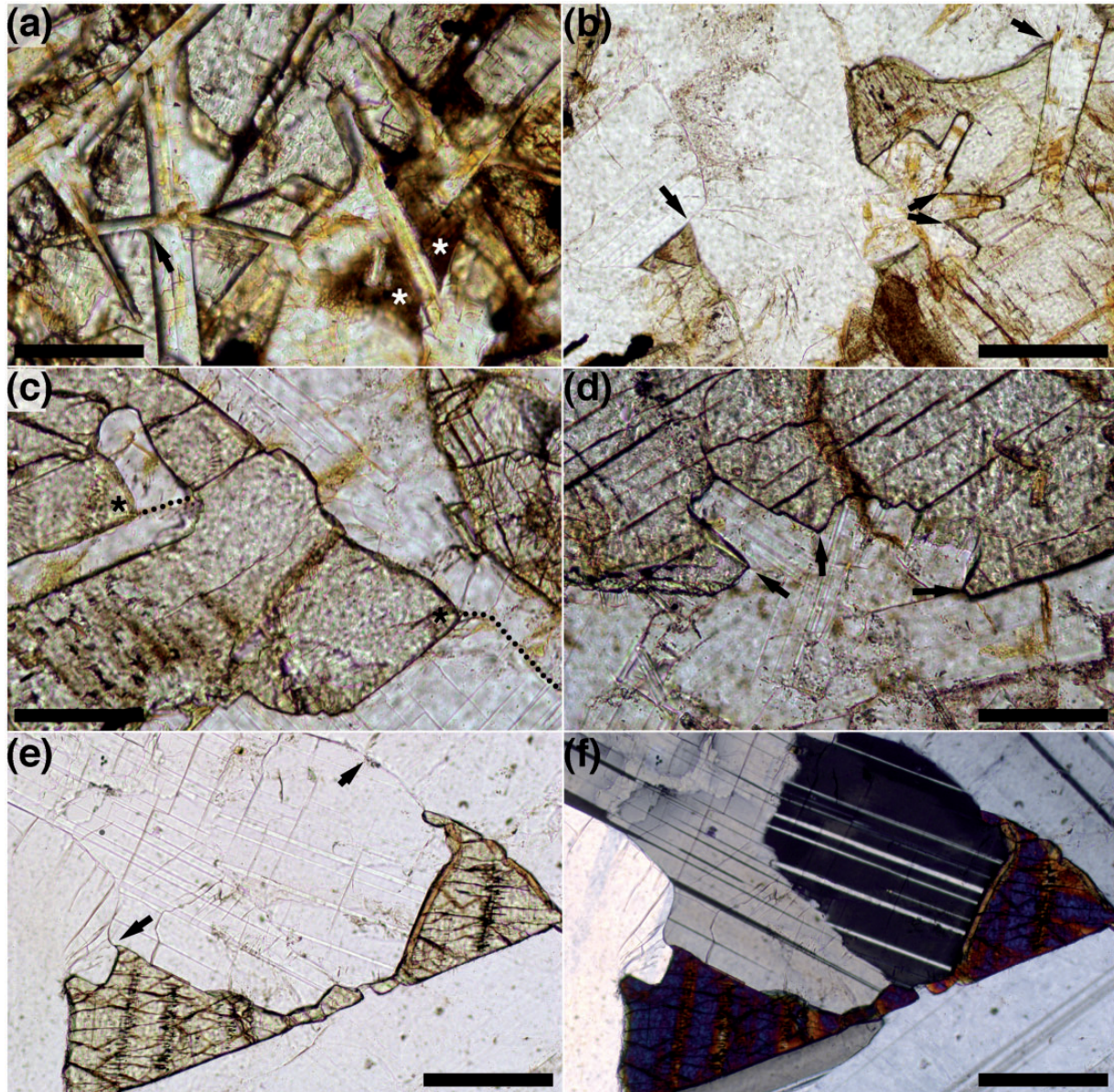
Fig. 1. Photomicrographs of microstructures in mafic rocks. All images are dominated by augite (high relief) and plagioclase (clear). (a) Sample ROM48-32 from the ∼3 m thick Traigh Bhàn na Sgùrra sill (Holness & Humphreys, 2003; Holness *et al.*, 2012*b*) (plane-polarized light). The augite infills the spaces between the plagioclase laths, with almost perfect pseudomorphing of the original melt-filled spaces. Silica-rich glass is present in some pores (examples are marked with an asterisk). The arrow points to the corner of a pore that is incompletely filled with augite. Scale bar is 100 μm long. (b) Sample 87-95 from close to the margin of the 130 m thick Portal Peak Sill (Holness *et al.*, 2012*b*) photographed in plane-polarized light. The augite–plagioclase–plagioclase dihedral angles are formed by the meeting of planar augite–plagioclase grain boundaries (examples are arrowed), demonstrating almost perfect pseudomorphing of the melt by augite and therefore minimal growth of the plagioclase walls. Scale bar is 200 μm long. (c) Sample 87-106 from the centre of the Portal Peak Sill (plane-polarized light). The two augite–plagioclase–plagioclase three-grain junctions (both marked with an asterisk) are formed by the meeting of curved augite–plagioclase grain boundaries (the plagioclase–plagioclase grain boundaries are marked by dotted lines in each case). This is because infilling of the melt-filled pore occurred by simultaneous growth of the two phases. Scale bar is 200 μm long. (d) Sample 87-110 from the centre of the Portal Peak Sill, showing further examples (arrowed) of high dihedral angles caused by simultaneous growth of augite and plagioclase. Scale bar is 200 μm long. (e, f) Sample 118681 from LZa of the Skaergaard intrusion [plane-polarized light in (e), crossed polars in (f)]. Noteworthy features are the localized rim of brown amphibole on the augite (e) and the asymmetry of the three-grain junctions [an example on the left-hand side of the images is arrowed in (e)]. The plagioclase–plagioclase grain boundary marked in (e) with an arrow is not parallel to the growth twins [visible in (f)], and is marked by compositional zoning of the grain below the boundary. The position of the grain boundary is therefore likely to be original, demonstrating the primary igneous nature of the three-grain junctions in this example. Scale bar in both images is 200 μm long.

crystal growth rates have been published (e.g. Cashman, 1993) none have specifically addressed the issue of growth rates in small pores and so the exact control on the inferred change of relative growth rates of the plagioclase and augite remains unknown. Notwithstanding the precise mechanisms effecting the change, Θ_{cpp} varies symmetrically across essentially unfractionated sills, with low values at the rapidly cooled margins and higher values in the more slowly cooled centre (Fig. 2). Θ_{cpp} is a sensitive function of the time taken to crystallize (Holness et al., 2012b).

The corollary of the new work presented by Holness et al. (2012a, 2012b) is that Θ_{cpp} in mafic rocks is part of the primary igneous microstructure and provides a record of processes that occur during solidification. Sub-solidus modification of three-grain junctions involving more than one phase is generally limited in many kilometre-scale coarse-grained intrusions, with significant changes of Θ_{cpp} occurring only in fine-grained mafic rocks that remained hot for long periods, such as chill zones in large intrusions, and in the interiors of oikocrysts (Holness et al., 2012a). Holness et al. (2012a) discussed the microstructures associated with late liquid infiltration and argued that they are clearly distinct from those seen in most mafic rocks.
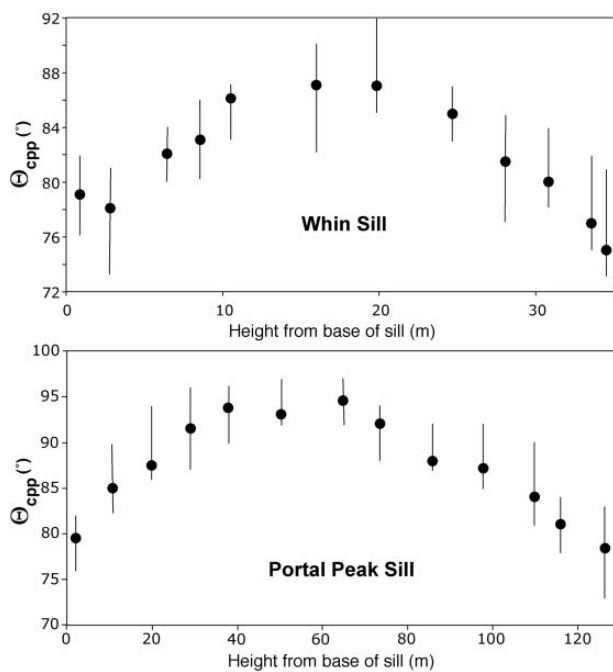
Fig. 2. Variation of Θ_{cpp} across the Whin Sill of Northern England, and the Portal Peak Sill of Antarctica. [See Holness et al. (2012a, 2012b) for more details of these intrusions.] The median value is that of populations of 100 measurements for each sample, and the error bars give the 95% confidence intervals calculated according to the method of Stickels & Hücke (1964). The symmetric variation of Θ_{cpp} across each sill should be noted. This is in marked contrast to the variation of plagioclase grain size, which reaches a maximum above the centre point (Holness et al., 2012b).

In this contribution we present data from the Bushveld Complex and Sept Iles Intrusion, and re-examine data from the Rum and Skaergaard intrusions. We argue that the previously reported stepwise variation of Θ_{cpp} in Skaergaard cumulates is common to all mafic layered intrusions and reflects fundamental processes occurring during magma fractionation.

METHODS

Most published work on dihedral angles, including this contribution, reports the median of angle populations, primarily because the median can be determined to within a few degrees with a relatively small number of single measurements (Riegger & van Vlack, 1960). Although much of the early work on dihedral angles in geological systems was based on populations of apparent angles measured on a flat rotating stage [although see Voll (1960) and Vernon (1968) for exceptions], measurement on a universal stage permits us to use the information encoded in the population of true angles (e.g. Holness, 2010).

There are several possible sources of uncertainty in determining the dihedral angle distribution. The first is a simple measurement bias, with undue emphasis given to angles in a particular size range. The universal stage provides a useful check on this possibility, because the true value of the angle can be determined only when it is correctly oriented. There is also an uncertainty associated with the measurement of each angle, and this is typically of the order of a few degrees (e.g. Gleason et al., 1999). The final source of uncertainty is because we do not know the distribution function of the underlying (parent) population that is being sampled, so it is not straightforward to work out the uncertainty on the median or standard deviation of a randomly chosen sub-group of this population. Stickels & Hücke (1964) developed a non-parametric method, based on the assumption that the population has a continuous distribution function of some unknown form, to establish the confidence intervals for the median angle of a population independent of its actual distribution.

The uncertainty on Θ_{cpp} decreases as the number of measurements is increased, although it remains relatively high for samples in which there is a great spread of angles. Much of the earlier published work on the Skaergaard and Rum cumulates was dominated by values of Θ_{cpp} based on ~30 measurements (e.g. Holness et al., 2007a, 2007b), and the (unreported) uncertainties on these measurements may be high, leading to variability of Θ_{cpp} between related samples. As part of this study we revisited many of the original data and added more measurements. This resulted in 2σ values typically of the order $\pm3°$ or less and a reduction in variability between closely spaced samples.

In this study we measured at least 50 dihedral angles in each sample to obtain the median, using the method of Stickels & Hücke (1964) to constrain the 95% confidence

interval. Holness (2010) demonstrated that ~100 measurements are required to place good constraints (i.e. of the order ±2°) on the standard deviation. Although we report the standard deviation for all our samples, we will discuss only the standard deviations of those samples for which we have ~100 measurements. We report the skew for our angle populations but do not place much confidence on these values. Approximately 50 measurements give a good idea of the median (which is similar to the first moment of the distribution), and ~100 measurements are needed to constrain the standard deviation (the second moment of the distribution). We therefore anticipate that many more than 100 measurements are required to constrain the skew (the third moment).

A summary of our results is given in Tables 1–4, with the full datasets available as Supplementary Data (available for downloading at http://www.petrology.oxfordjournals.org).

LAYERED MAFIC INTRUSIONS

This study concentrates on a group of four mafic layered intrusions. They range in size from 10 km to 350 km diameter. Whereas all were formed by the solidification of basaltic magma, in detail the liquid lines of descent were different in each, with different sequences of arrival of cumulus minerals and differences in the interstitial mineral assemblages (e.g. some contain abundant late-stage replacive or primary amphibole) and by the variable presence of late-stage reactive microstructures indicative of the development of immiscibility of the interstitial liquid (e.g. Holness *et al.*, 2011; Namur *et al.*, 2012).

The Eastern Layered Intrusion of Rum, Inner Hebrides

Geological setting

The Paleocene Rum Igneous Complex comprises several distinct intrusive bodies, together with a suite of early silicic extrusive and intrusive rocks (Emeleus *et al.*, 1996). It represents the exhumed, shallow-crustal roots of a former shield volcano. The Eastern Layered Intrusion is semi-circular in plan view, with a radius ~4 km from east to west, and a diameter about 6 km north to south (Emeleus, 1997). The exposed stratigraphy is 700 m thick. It is divided into 16 cyclic units, each comprising an olivine-rich horizon and an overlying plagioclase-rich horizon that may be troctolite or olivine gabbro (the local term for these plagioclase cumulates is allivalite). Some of these cyclic units may represent the accumulation of crystals from a single

Table 1: Dihedral angle data for allivalites of the Rum Eastern Layered Intrusion

Sample	Height	n	Θ_{cpp}	SD	Skew	Old Θ_{cpp}	Notes
Unit 12 allivalite (troctolite)							
R12-J4	2·65	100	83·5 ± 4·5	22·5	−0·34	84	Immediately underlying a minor peridotite horizon (SPII)
R12-J5	4·62	100	79 ± 4	23·4	0·08	81	Immediately overlying a minor peridotite horizon (SPII)
R12-J6	5·75	100	80 ± 4	22·4	−0·02	80	
R12-J7	6·40	100	79 ± 2·5	21·7	−0·53	77·5	
R12-J8	6·95	100	87·5 ± 4	17·5	−0·11	88	Immediately underlying a minor peridotite horizon (SPIII)
R12-J10	8·40	100	82 ± 4	21·5	−0·78	80·5	
R12-J12	10·30	100	80 ± 3·5	20·8	−1·05	80	
R12-J13	11·40	100	82·5 ± 4	19·9	−0·29	81	
R12-J15	13·71	100	89·5 ± 3·5	17·2	−0·29	89	Immediately underlying a minor peridotite horizon (SPV)
Unit 8/9 allivalite (gabbro)							
F5	2·30	100	90 ± 2	13·3	−0·23	90	
F11	9·55	100	91 ± 1·5	15·4	−1·39	91	
F12	11·45	100	90 ± 2	16·4	−0·65	88	
F20	23·80	100	91 ± 3	14·9	−0·67	89	
F21	25·20	100	91 ± 3	14·0	−0·54	90	
F25	36·40	100	91·5 ± 3·5	18·2	−1·10	87	

Height gives the height (in metres) above the base of the allivalite horizon (the Unit 12 allivalite for the R12 samples, and the Unit 8/9 allivalite for the F samples); n is the number of dihedral angle measurements. The errors on Θ_{cpp} are the 95% confidence interval calculated according to Stickels & Hücke (1964). The error on the standard deviation is likely to be of the order of ±1° [from the results of Holness (2010)]. Old Θ_{cpp} gives the values previously reported by Holness & Winpenny (2009) (for the R12 samples), and Holness *et al.* (2007*a*) (for the F samples). These previously reported values were based on populations of 30 measurements.

Table 2: Dihedral angle data for cumulates of the Skaergaard Layered Series

Sample	Height	Rock type	Unit	n	Θ_{cpp}	SD	Skew	Old Θ_{cpp}	Sample source
118741	35	po-C	HZ	100	79 ± 3·5	19·3	−0·61	76·5 (30)	Cambridge drill core
118738	50	po-C	HZ	100	77 ± 3·5	19·4	−0·62	72·5 (30)	Cambridge drill core
118736	63	po-C	HZ	100	83 ± 3·5	18·3	0·30	84·5 (50)	Cambridge drill core
118734	71	po-C	HZ	100	96·5 ± 3	17·3	−0·34	95·5 (30)	Cambridge drill core
118714	133	po-C	HZ	60	83·5 ± 3	19·62	−0·38	81 (30)	Cambridge drill core
870′2″	181	po-C	LZa	60	86 ± 2	14·0	0·59	89·5 (28)	Cambridge drill core
118694	200	po-C	LZa	106	84 ± 3	17·0	−1·11	81 (30)	Cambridge drill core
118676	287	po-C	LZa	60	85 ± 2·5	12·3	−0·83	79·5 (30)	Cambridge drill core
661′2″	319	po-C	LZa	100	96 ± 1·5	14·3	0·11	93 (30)	Cambridge drill core
458242	381	po-C	LZa	100	84 ± 2	15·5	−0·45	78·5 (30)	Tegner reference profile
458213	505	po-C	LZa	100	83·5 ± 2	14·7	−0·27	83 (30)	Tegner reference profile
458215	569	poc-C	LZb	100	100 ± 2	13·5	−0·67	100·5 (30)	Tegner reference profile
458216	591	poc-C	LZb	100	101 ± 2	14·0	−1·97	104 (30)	Tegner reference profile
118614	649	poc-C	LZb	100	99 ± 3	12·7	−1·29	101 (30)	Cambridge drill core
118589b	726	poc-C	LZb	100	99 ± 2	12·5	−0·09	100 (30)	Cambridge drill core
458226	837	poc-C	LZb	99	97 ± 2	13·0	−0·89	98 (30)	Tegner reference profile
458231	922	poc-C	LZb	100	100 ± 2	11·2	−0·39	100 (30)	Tegner reference profile
458201	1062	poc-C	LZb	100	99 ± 2	11·3	−1·13	99 (30)	Tegner reference profile
458203	1143	poc-C	LZb	100	98·5 ± 2	12·4	−1·35	96·5 (30)	Tegner reference profile
SKG11-33	1375	poc-C	LZb	50	95·5 ± 3	8·0	−0·35	—	New surface sample
SKG11-34	1377	pocmi-C	LZc	50	100 ± 3	9·0	−0·53	—	New surface sample
458285	1517	pocmi-C	LZc	100	99 ± 2	11·2	−1·53	102 (30)	Tegner reference profile
SK-366	1964	pcmi-C	MZ	100	100 ± 2	12·0	−0·30	100·5 (20)	Bollingberg collection
873·7 m	2138	pocmi-C	UZa	100	99 ± 2	14·6	−1·54	99·5 (30)	Platinova 90-22 drill core
660·6 m	2322	pocmi-C	UZa	100	98 ± 2	13·7	−1·22	99 (30)	Platinova 90-22 drill core
585·8 m	2386	pocmi-C	UZa	100	97 ± 2·5	13·3	−0·78	97·5 (20)	Platinova 90-22 drill core
485 m	2473	pocmi-C	UZa	100	80 ± 4	13·5	0·46	80 (26)	Platinova 90-22 drill core
483·3 m	2475	pocmi-C	UZa	100	83 ± 2·5	16·1	−1·20	—	Platinova 90-22 drill core
475 m	2483	pocmia-C	UZb	50	103 ± 2·5	12·0	−0·72	105 (30)	Platinova 90-22 drill core
421 m	2532	pocmia-C	UZb	100	80·5 ± 4	18·2	−0·05	75 (20)	Platinova 90-22 drill core
364·1 m	2585	pocmia-C	UZb	100	80 ± 3	20·0	−0·34	76 (20)	Platinova 90-22 drill core
323·8 m	2622	pocmia-C	UZb	95	82 ± 4	22·9	−0·61	79·5 (20)	Platinova 90-22 drill core
SK-372	2668	pocmia-C	UZb	100	79·5 ± 3·5	20·5	−1·03	78·5 (30)	Bollingberg collection
210·9 m	2727	pocmia-C	UZb	100	82 ± 4	23·0	−0·82	77 (30)	Platinova 90-22 drill core
SK-374	2820	pocmia-C	UZb	100	79 ± 4·5	22·4	0·00	77 (30)	Bollingberg collection
87·7 m	2841	pocmia-C	UZb	100	79 ± 4	22·5	−0·39	80 (30)	Platinova 90-22 drill core
47·7 m	2879	pocmia-C	UZc	91	80 ± 5	22·6	−0·48	71·5 (30)	Platinova 90-22 drill core
SK84-376	3003	pocmia-C	UZc	91	79 ± 3	22·3	−0·67	75·5 (30)	Bollingberg collection

Height gives the height (in metres) above the presumed base of the intrusion; rock type follows the scheme of Irvine (1982) (p, plagioclase; o, olivine; c, clinopyroxene; m, magnetite; i, ilmenite; a, apatite; -C, cumulus); n is the number of dihedral angle measurements. The errors on Θ_{cpp} are the 95% confidence interval calculated according to Stickels & Hücke (1964). The error on the standard deviation is likely to be of the order of $\pm 1°$ [from the results of Holness (2010)]. Data for each sample ('Old Θ_{cpp}') have previously been reported by Holness *et al*. (2007*b*), but for smaller values of n (given in parentheses).

Table 3: Dihedral angle data for the Upper Zone of the Bushveld Complex, as sampled by the Bierkraal drill cores

Sample	Depth (m)	Rock type	Unit	n	Θ_{cpp}	SD	Skew	P_2O_5
2W 481.9	2122·9	phc-C	MZ$_u$	100	85 ± 1·5	13·8	−0·18	—
2W 448	2091·9	phc-C	MZ$_u$	100	84 ± 2	15·3	−0·28	—
2W 402	2049·9	phc-C	MZ$_u$	95	85 ± 2·5	12·3	0·26	—
2W 324	1978·6	phc-C	MZ$_u$	57	85 ± 1·5	10·8	−0·43	—
2W 225	1888·2	phc-C	MZ$_u$	62	85 ± 1·5	10·4	−1·19	—
3W 1275	1744·8	phcmi-C	UZa	60	90·5 ± 2·5	7·0	0·39	0·04
3W 1268.9	1739·2	phcmi-C	UZa	60	91 ± 2	9·4	−0·08	0·01
3W 1212.25	1687·5	phcmi-C	UZa	94	90 ± 2	11·1	0·34	0·02
3W 938	1436·9	pohcmi-C	UZb	50	90 ± 2	8·6	−0·39	0·02
3W 640.9	1165·5	pohcmi-C	UZb	71	91 ± 2	8·5	−1·19	0·05
1W 1550.7	1037·5	pocmia-C	UZc	60	96·5 ± 2	8·3	0·02	3·49
3W 430.0	972·9	pocmia-C	UZc	48	91 ± 2	12·6	−0·83	0·11
1W 1423.4	921·2	pocmia-C	UZc	60	96 ± 2	10·4	−0·94	6·77
3W 300	854·1	pocmi-C	UZc	100	91 ± 2	8·8	0·05	0·17
1W 1329.2	835·1	pocmia-C	UZc	77	97 ± 2	8·5	−0·66	1·87
1W 1239.5	752·8	pocmia-C	UZc	63	96 ± 1·5	7·8	−0·05	1·46
1W 1199.2	716·4	pocmia-C	UZc	70	95 ± 2	7·7	−0·57	0·80
1W 1138.2	660·6	pocmi-C	UZc	100	92 ± 1·5	6·2	0·41	0·11
1W 1010.2	543·7	pocmia-C	UZc	71	96 ± 2·5	8·2	1·05	1·23
1W 908.6	450·9	pocmia-C	UZc	30	96 ± 2	6·5	0·37	0·14
1W 808.6	359·6	pocmia-C	UZc	50	96 ± 1·5	9·7	−0·33	1·13

The depth (in metres) is measured from the base of the overlying granite, using the correlation of Kruger *et al.* (1987) to link the three drill cores. Rock type follows the scheme of Irvine (1982), with h denoting orthopyroxene (all other abbreviations as Table 2); *n* is the number of dihedral angle measurements. The errors on Θ_{cpp} are the 95% confidence interval calculated according to Stickels & Hücke (1964). The error on the standard deviation is of the order of ±1° for those samples with populations of 100, and of the order of ±2–3° for samples with 50 measurements [estimated from the results of Holness (2010)]. The bulk-rock P_2O_5 content (in wt %), where reported, is taken from Tegner *et al.* (2006).

batch of fractionating magma, but most are built of successive layers formed from many smaller replenishments of picritic or basaltic magma into a repeatedly reconstituted sill-like chamber (Renner & Palacz, 1987; Emeleus *et al.*, 1996; Holness & Winpenny, 2009). Locally there is clearly recognizable evidence of upwards migration into the base of the allivalites of late-stage liquids sourced from the underlying peridotite, including fingered replacement features (Butcher *et al.*, 1985; Morse *et al.*, 1987), wholesale mobilization of cumulus augite (Holness *et al.*, 2007*c*), cryptic features such as changes in mineral composition (Tait, 1985) and the development of cuspate augite grains at three-grain junctions between plagioclase (Fig. 3c; Holness, 2007; Sides, 2008; Holness *et al.*, 2012*a*).

Petrography

The troctolitic allivalites contain primocrysts of olivine and plagioclase. Neither mineral has significant compositional zoning. Minor primocrystic Cr-spinel may be present. Minor interstitial augite forms thin monocrystalline rims around olivine primocrysts (Fig. 3a). The gabbroic allivalites contain equant primocrysts of augite in addition to olivine and plagioclase (Fig. 3b). Augite–plagioclase grain boundaries are generally curved in the immediate vicinity of three-grain junctions (denoting simultaneous growth of the two minerals), often with some asymmetry at the junction itself (Fig. 3b). Local infiltration of liquid derived from the underlying peridotite is recorded in clearly identifiable cuspate extensions to cumulus augite grains (Fig. 3c). Both types of allivalite may have a strong igneous foliation defined by preferred alignment of plagioclase. The peridotites of the Eastern Layered Intrusion contain a few volume per cent of late-stage magmatic phases such as biotite and amphibole, but these phases are not present in either the troctolites or the gabbros: the allivalites are close to endmember adcumulates.

Choice of samples

We chose samples from the allivalites of two of the cyclic units, avoiding those in which late-stage infiltration

Table 4: Dihedral angle data for MCU-1 of the Sept Iles Intrusion

Sample DC9-	Height (m)	Rock type	n	Θ_{cpp}	SD	Skew
2410·0	−4108·4	po-C	50	84 ± 3	10·1	−0·47
2382·5	−4085·9	po-C	50	83 ± 2	13·0	−0·84
2363·5	−4070·3	po-C	50	85·5 ± 2·5	12·7	0·57
2202·5	−3938·5	po-C	50	85·5 ± 3·5	13·5	0·19
1920·5	−3707·2	po-C	46	84·5 ± 3·5	13·2	−0·63
1874·5	−3669·6	pomi-C	50	94 ± 3·5	11·2	−0·35
1855·0	**−3653·6**	**pomi-C**	**50**	**93 ± 2**	**10·9**	**−1·21**
1833·5	−3636·0	pomi-C	50	93 ± 1·5	7·3	0·18
1804·0	−3611·8	pomi-C	30	94·5 ± 4	9·3	0·30
1717·5	−3540·9	pomi-C	50	92·5 ± 3·5	10·6	0·43
1604·0	−3447·9	pomi-C	39	94 ± 2	9·3	−1·40
1599·5	−3444·2	pomi-C	30	95 ± 3·5	9·9	0·43
1514·5	−3374·5	pomic-C	50	104 ± 2	8·7	−0·13
1469·5	−3337·7	pomic-C	50	102 ± 2·5	8·5	−0·89
1341·0	−3232·3	pomic-C	50	105 ± 4	10·8	0·06
1261·0	−3167·2	pomic-C	50	103 ± 2·5	8·5	−0·42
1143·0	−3069·0	pomic-C	50	103·5 ± 2·5	8·9	−0·84
1081	−3019·3	pmic-C	50	99 ± 3	12·7	−1·79
1045·5	−2990·2	pmic-C	50	97 ± 2·5	14·7	−0·85
891·5	−2864·0	pmic-C	50	97·5 ± 2·5	13·9	−1·13
740·5	−2740·2	pmic-C	38	98 ± 4	10·0	0·97
650	−2666·1	pmic-C	50	98 ± 1·5	10·2	−1·99
559	−2591·5	pmic-C	50	102 ± 2	11·1	−0·14
493·5	−2537·8	pomica-C	50	102 ± 4	11·7	−1·09
429	−2485·0	pomica-C	50	100 ± 2·5	11·6	−0·04
359·5	−2457·5	pomica-C	50	102 ± 2	8·5	−0·85

The sample number is the depth (in metres) of each sample in the drill core; the height is the stratigraphic height of each sample according to the scheme of Namur *et al.* (2010); rock type follows the scheme of Irvine (1982); *n* is the number of dihedral angle measurements. The errors on Θ_{cpp} are the 95% confidence interval calculated according to Stickels & Hücke (1964). The error on the standard deviation is likely to be of the order of ±2–3° [estimated from the results of Holness (2010)]. The data for DC9-1855.0 (given in bold type) are for orthopyroxene–plagioclase–plagioclase junctions.

metasomatism has been documented (Holness, 2007; Holness *et al.*, 2007*c*, 2012*a*; Holness & Winpenny, 2009). The allivalite of Unit 12 is 13·5–17·5 m thick where it crops out on the eastern side of the intrusion. It is dominated by foliated troctolites and contains five minor peridotite horizons ranging from 20 cm to 2·4 m thick, denoted SPI to SPV by Holness & Winpenny (2009). Θ_{cpp} is locally elevated immediately below SPIII and SPV (i.e. within a

few centimeters of the contact), most probably because of the thermal effects associated with chamber replenishment by hot primitive magma (Holness & Winpenny, 2009). Low Θ_{cpp} values, associated with the cuspate grains of interstitial augite that are a key indicator of infiltration of late-stage liquids, are locally found in the lowermost 3 m of the allivalite unit (Fig. 3c). We chose a subset of samples from Traverse J of Holness & Winpenny (2009), collected from grid reference [39 231, 95 888], avoiding samples from the lowermost 3 m, but including three samples from immediately below three of the minor peridotites.

Unit 8/9 is a complex unit that was locally intruded by a discontinuous picrite sill, now forming the Unit 9 peridotite. The intrusion of this body of primitive liquid resulted in large-scale mobilization of augite within the overlying allivalite, forming the well-known Wavy Horizon (Holness *et al.*, 2007*c*) separating the metasomatized troctolite from the relatively unaffected overlying gabbro. Where not intruded by the Unit 9 peridotite, the allivalites of Unit 8 and 9 merge into a single (unmetasomatized) gabbroic allivalite, ∼44 m thick; Holness *et al.* (2007*c*) called this merged unit the Unit 8/9 allivalite. We chose a suite of samples from the Unit 8/9 allivalite, far from any evidence of metasomatic alteration, from Traverse f (Holness *et al.*, 2007*c*) located at grid reference [39 940, 96 558].

Median dihedral angles have previously been reported for all samples examined as part of this study, although Θ_{cpp} was based on only 30 measurements in each sample. Here we measured 100 three-grain junctions to determine both Θ_{cpp} and the standard deviation of the population. The results are given in Table 1, together with the previously reported values of Θ_{cpp} for comparison.

The Skaergaard intrusion, East Greenland
Geological setting
The Skaergaard intrusion formed from the injection of a large (8 km × 11 km × 4 km) body (Nielsen, 2004) of relatively evolved tholeiitic basalt into a fault-bounded space (Irvine *et al.*, 1998) in the extending crust of East Greenland during the opening of the North Atlantic. The intrusion lies at the unconformity between underlying Precambrian gneisses and an overlying sequence of Eocene plateau lavas (Wager & Deer, 1939). After filling, the chamber remained closed both to further magma replenishment and to eruption, forming an excellent example of extreme fractionation of basaltic magma.

Solidification resulted in the formation of three series, first defined by Wager & Deer (1939): the (volumetrically dominant) Layered Series (LS) crystallized upwards from the floor, the Marginal Border Series (MBS) crystallized inwards from the (vertical) walls, and the Upper Border Series (UBS) crystallized downwards from the roof. The LS and UBS meet at the Sandwich Horizon. The LS is
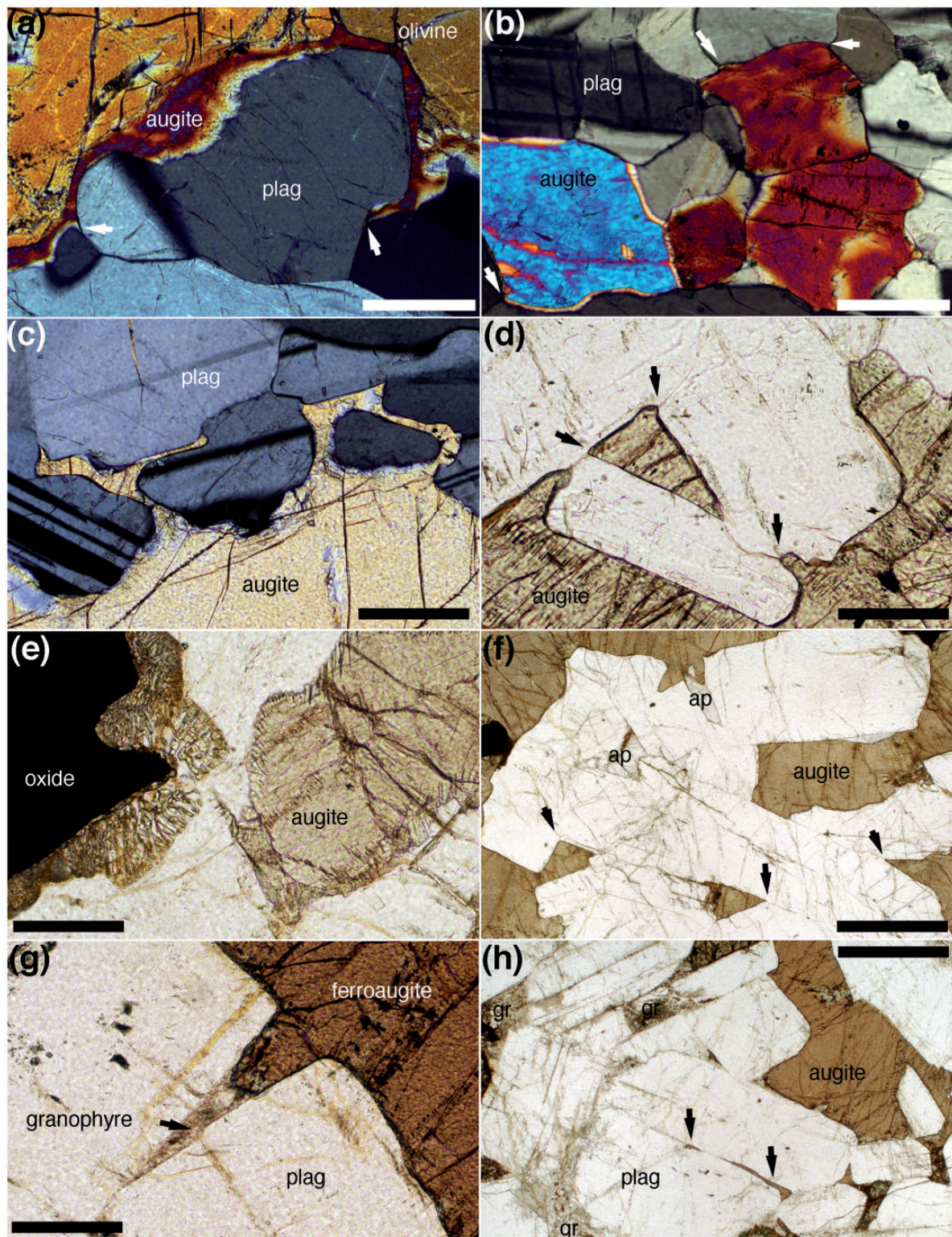
Fig. 3. Photomicrographs of selected microstructures. (a) Sample R12-J12 from the Unit l2 allivalite of the Rum Eastern Layered Intrusion (crossed polars). Cumulus olivine grains typically have thin monocrystalline rims of augite separating them from cumulus plagioclase. The low dihedral angles (arrowed) should be noted. Data for this sample are presented in Table 1. Scale bar is 200 µm long. (b) Sample N48 from the Unit l0 allivalite [described by Holness *et al.* (2012a)] (crossed polars). This is a gabbroic cumulate with equant primocrysts of augite. The high dihedral angles (arrowed) should be noted. Θ_{cpp} for this sample is $91° \pm 3·5°$. The scale bar is 200 µm long. (c) Sample N32 from the

(continued)

divided into Lower, Middle and Upper Zones based on the absence of cumulus olivine in the Middle Zone. The Lower Zone is further subdivided: LZa contains cumulus olivine and plagioclase, the base of LZb is marked by the arrival of cumulus augite, and the base of LZc is marked by the arrival of cumulus Fe–Ti oxides. The Upper Zone is also subdivided; the base of UZb defines the arrival of cumulus apatite, whereas the base of UZc marks the first appearance of the mosaic form of ferro-hedenbergite inverted from β-ferrobustamite. The UBS (Naslund, 1984; Salmonsen & Tegner, 2013) and MBS (Hoover, 1989) can be similarly subdivided.

Petrography

Plagioclase and clinopyroxene (augite near the base, and ferroaugite at the top of the stratigraphy) are present throughout the Layered Series. In LZa augite is present as an interstitial, commonly poikilitic, phase, but the augite becomes more compact and volumetrically more important over a transitional zone into LZb. The precise stratigraphic height at which it joins the cumulus assemblage is not known, but it is conventionally placed 175 m above the base of the exposed stratigraphy. Low-Ca pyroxene (inverted pigeonite) is present up to the middle of UZa: the experiments of Thy *et al.* (2006) suggested that low-Ca pyroxene becomes a liquidus phase after liquid saturation in oxides (i.e. within LZc), in keeping with the conclusion of Toplis *et al.* (1994). However, Wager & Brown (1968) stated that 'cumulus' pigeonite is erratically present from 500 m stratigraphic height (i.e. in the upper part of LZb).

Augite–plagioclase grain boundaries in the lower parts of the Layered Series are curved in the immediate vicinity of the three-grain junctions, often with some asymmetry (Figs 1e, f and 3d), and commonly have compositionally zoned plagioclase immediately adjacent to the junction (Fig. 1f). The sense of the asymmetry is generally such that the convex grain boundary involves that plagioclase grain whose (010) face defines the orientation of the plagioclase–plagioclase grain boundary.

In LZc and MZ, augite–plagioclase grain boundaries develop serrations associated with the formation of elongate irregular extensions of augite down plagioclase–plagioclase grain boundaries (Fig. 3e). These features are the stepped grain boundaries and fish-hook pyroxenes of Holness *et al.* (2011) and are caused by reaction with late-stage liquids.

The curvature of augite–plagioclase grain boundaries at three-grain junctions is absent above the upper parts of UZa (Fig. 3f), apart from a short stratigraphic interval immediately above the arrival of cumulus apatite. In this upper part of the stratigraphy, the three-grain junctions are formed by the intersection of planar augite–plagioclase grain boundaries. The change to planar grain boundaries results in a decrease in Θ_{cpp} and is associated with a tendency for all mafic phases to fill small interstitial pockets between plagioclase grains (Fig. 3h).

A further feature of note is a change in morphology of apatite, which is interstitial throughout the stratigraphy until UZb where it joins the cumulus assemblage. In LZa, interstitial apatite is generally anhedral, although euhedral grains are locally present (Fig. 4a). Apatite changes from anhedral to euhedral in LZb (Fig. 4b and c). It remains euhedral until the upper part of UZa where significant numbers of anhedral grains are present together with a few euhedral grains (Figs 3f and 4d). Apatite is entirely euhedral once it joins the cumulus assemblage at the base of UZb.

The rocks of LZa are orthocumulates, with up to 45% trapped liquid (Tegner *et al.*, 2009) that crystallized abundant interstitial augite, biotite, apatite, low-Ca pyroxene, and oxides in addition to overgrowths on the olivine and plagioclase cumulus grains. The augite commonly has localized overgrowth rims of brown amphibole (Fig. 1e). The lower parts of LZb are similarly orthocumulates but

Fig. 3 Continued

Unit 10 allivalite [described by Holness *et al.* (2012*a*)] (crossed polars). In contrast to (b), this sample experienced infiltration metasomatism. Crystallization of the infiltrating liquid formed elongate extensions to the original cumulus grains, and $\Theta_{cpp} = 72 \cdot 5° \pm 3°$. The scale bar is 200 μm long. (d) Sample 458 216 from LZb of the Skaergaard Layered Series (plane-polarized light). It should be noted that the three-grain junctions (arrowed) involve curvature of the otherwise generally planar augite–plagioclase boundaries, resulting in a higher angle than would be expected if the augite were simply pseudomorphing the original melt-filled space between the two plagioclase grains. Data for this sample are presented in Table 2. Scale bar is 200 μm long. (e) Sample 458 277 from LZb of the Skaergaard Layered Series (plane-polarized light). The oxide grain is surrounded by a symplectite of pyroxene and Fe-rich plagioclase that is replacing the adjacent plagioclase primocryst. The serrations at the margins of the cumulus augite (stepped grain boundary) should also be noted. These features are indicative of late-stage reactive liquids, and the symplectites have been attributed to reaction of an Fe-rich liquid subsequent to the loss of an immiscible silica-rich conjugate (Holness *et al.*, 2011). Scale bar is 200 μm long. (f) Sample 483·3 m from the 90-22 drill core sampling UZa of the Skaergaard Layered Series (plane-polarized light). The augite–plagioclase grain boundaries are planar and there is no curvature at three-grain junctions, leading to low Θ_{cpp} (83° $\pm 2 \cdot 5°$). It should be noted also that the interstitial apatite is anhedral, with a shape determined by the bounding plagioclase grains. The apatite grains in the centre of this image are reproduced at a higher magnification in Fig. 4d. Data for this sample are presented in Table 2. (g) Sample 47·4 m from the 90-22 drill core sampling UZc of the Skaergaard Layered Series (plane-polarized light). At this point in the stratigraphy the augite is very Fe-rich, giving the grains a strong brown colour in plane-polarized light. The granophyre filling the low-angle junction between two plagioclase grains should be noted. This feature is typical of rapidly cooled dolerites (Holness *et al.*, 2012*a*). Scale bar is 200 μm long. Data for this sample are presented in Table 2. (h) Sample 47·4 m from the 90-22 drill core sampling UZc of the Skaergaard Layered Series (plane-polarized light). The pockets of granophyre (gr) should be noted. Augite grows into small pores between plagioclase grains (arrowed). Scale bar is 1 mm long.
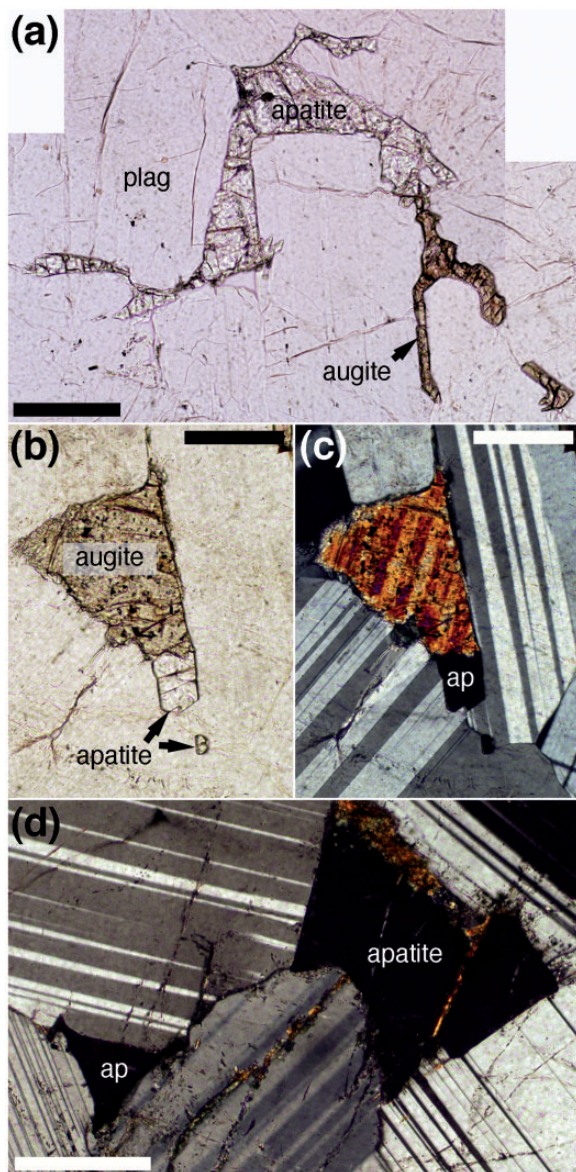
Fig. 4. The morphology of interstitial apatite in the Skaergaard Layered Series. Data from all samples are presented in Table 2. (a) Sample 118714 from the HZ. Many of the apatite grains in this sample are anhedral, with a shape defined by the bounding plagioclase primocrysts. Scale bar is 200 μm long. (b, c) Sample 458 285 from LZc. The invariably euhedral morphology of the interstitial apatite is clearly visible in plane-polarized light (b), whereas the position of the plagioclase–plagioclase grain boundaries is clear under crossed polars (c). Scale bar is 200 μm long in both images. (d) Sample 483·3 m from the 90-22 drill core (UZa) (crossed polars). The morphology of interstitial apatite is defined by growth faces of the bounding plagioclase grains. The larger-scale setting of this pair of apatite grains is shown in Fig. 3f. Scale bar is 200 μm long.

the amount of trapped liquid decreases through LZb to values of a few per cent (Tegner *et al.*, 2009). The overlying LZc and MZ are generally close to adcumulates, but the destabilization of a late-stage Fe-rich liquid by the loss of

its immiscible silica-rich conjugate is manifest by abundant reactive symplectites rooted on oxide grains (Fig. 3e; Holness *et al.*, 2011). These symplectites are absent above the base of UZb—here the interstitial liquid crystallizes as paired pockets of granophyre (Fig. 3g) and ilmenite-rich intergrowths, postulated to signify the retention of the silica-rich conjugate within the mush (Holness *et al.*, 2011). There is significant granophyre in the upper part of MZ and through the Upper Zone, in contradiction to the conclusions of Tegner *et al.* (2009), who suggested that the upper parts of the stratigraphy are adcumulate. Granophyre is commonly present at three-grain junctions, particularly where the two plagioclase grains meet at a low angle (Fig. 3g and h). The presence of granophyre in the narrow pores and the planar augite–plagioclase grain boundaries locally result in a microstructure highly reminiscent of those found in rapidly cooled dolerite sills (Fig. 3g).

Choice of samples

We chose a subset of samples for which dihedral angle data have previously been presented by Holness *et al.* (2007*b*). The samples were chosen to cover critical parts of the stratigraphy, including the step-changes and excursions of Θ_{cpp} documented by previous work. Few samples were selected for LZc and MZ because the great majority of three-grain junctions in this stratigraphic interval are affected by augite fish-hooks (Fig. 3e) and it is difficult to find samples with sufficient unaffected junctions to obtain statistically rigorous data. The sample suite includes material from the Cambridge drill core (this includes the only currently available material from the Hidden Zone, and covers LZa and the lowermost part of LZb; it forms part of the Harker Collection of the University of Cambridge), samples previously described by Tegner *et al.* (2009) for LZa up to MZ (the Tegner reference profile), samples collected by Karen Bollingberg (Bollingberg, 1995), and material from the 90-22 Platina drill core (this covers the upper part of MZ and continues to the middle of UZa; it is housed at GEUS in Copenhagen). We supplemented this sample set with two further samples (prefix SKG11) collected from the LZb–c boundary. We measured up to 100 three-grain junctions in each sample (using several thin-sections if necessary) to obtain the median dihedral angle, Θ_{cpp}, and the standard deviation. The results are given in Table 2.

The Bushveld Complex, South Africa

Geological setting

The ~2·06 Ga Bushveld Complex of South Africa is the largest known mafic layered intrusion on Earth. It intruded as a series of magma pulses, with the final major recharge event occurring within the Main Zone, about 4·2 km up in the 6·5 km stratigraphy. The incoming magma of this recharge event mixed with the resident

magma to form an essentially compositionally uniform body that was then closed to further magma input (von Gruenewaldt, 1973; Molyneux, 1974; Kruger *et al.*, 1987). The interval through which this recharge and mixing occurred includes the Pyroxenite Marker, a distinctive, thin, orthopyroxene-rich layer (von Gruenewaldt, 1970). Above this marker the stratigraphy is subdivided into Upper Main Zone (MZ_u), and then Upper Zone (UZ). Progressive fractionation resulted in evolution from a gabbronorite to an apatite–magnetite–fayalite ferrodiorite, with the sequential arrival of oxides (defining the top of MZ_u and the base of UZa), olivine (defining the base of UZb and associated with the loss of orthopyroxene) and apatite (defining the base of UZc) as cumulus phases. A detailed geochemical and petrographic study of the uppermost 2·1 km of layered mafic rocks sampled by three boreholes drilled in the western limb of the intrusion, at Bierkraal, detected at least nine distinct cycles marked by reversals in mineral composition and the intermittent presence of cumulus apatite and olivine (Tegner *et al.*, 2006). These cycles are attributed to periodic mixing driven by density inversion of a compositionally stratified magma body, triggered for at least two of these cycles by the crystallization of thick magnetite layers.

Petrography

We confined our study to the stratigraphy overlying the Pyroxenite Marker. The cumulates of MZ_u are dominated by cumulus plagioclase, augite and orthopyroxene, with interstitial Fe–Ti oxides, biotite and minor quartz. The plagioclase is commonly bent and deformed although the other phases show no signs of deformation. Undeformed interstitial quartz demonstrates that this deformation was super-solidus (Fig. 5a). Some samples are foliated, with a fabric defined by the preferred orientation of elongate plagioclase and pyroxene grains. The base of UZa is marked by a significant increase in the Fe–Ti oxide mode, although the habit of the Fe–Ti oxides may be
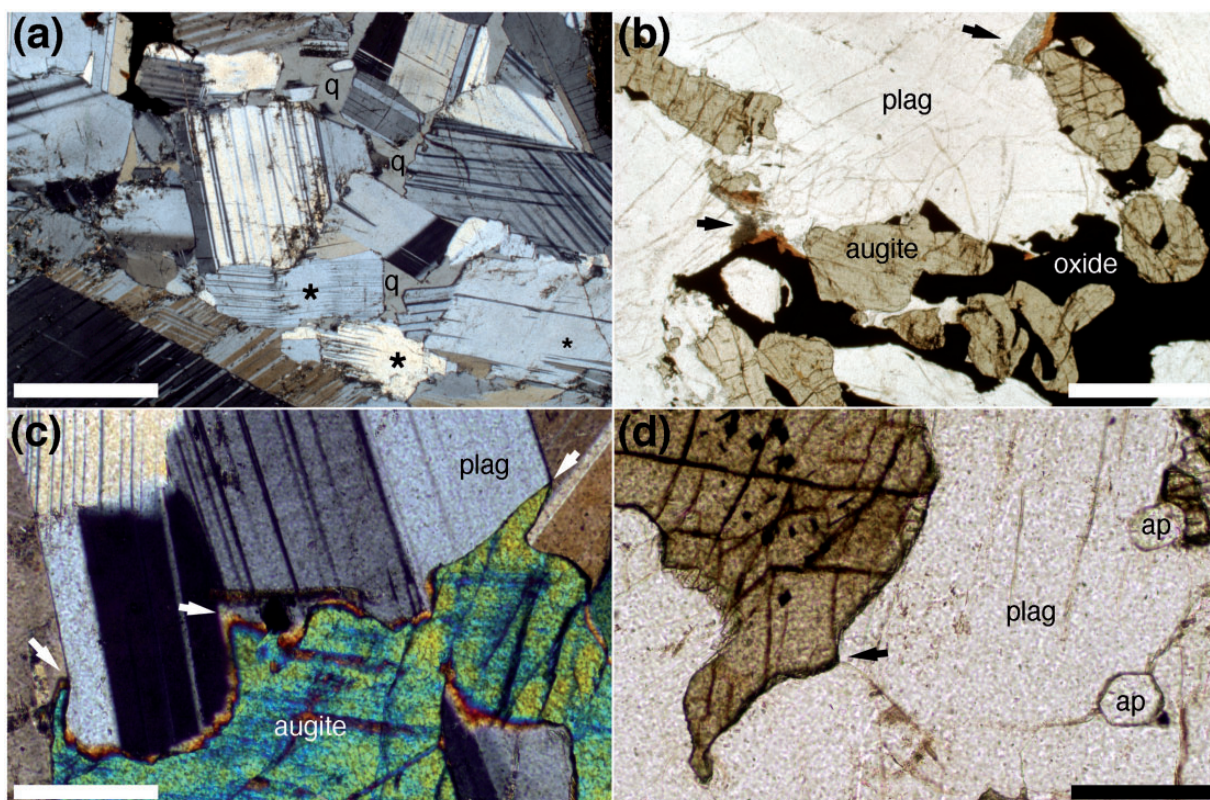
Fig. 5. (a) Sample 2W402 from the Bushveld Complex (crossed polars). Cumulus plagioclase grains are commonly bent (examples are marked with an asterisk), whereas the intercumulus quartz (q) is undeformed. Data for this sample are presented in Table 3. Scale bar is 1 mm long. (b) Sample 3Wl275 from the Bushveld Complex (plane-polarized light). The overall interstitial habit of the oxides, despite oxides being on the liquidus at this level in the stratigraphy, should be noted. Late-stage symplectites are arrowed. The thin rims of brown mica locally associated with the oxide should also be noted. Data for this sample are presented in Table 3. Scale bar is 1 mm long. (c) Sample 2W448 from the Bushveld Complex (crossed polars). Augite is cumulus in this sample from MZ_u. The low dihedral angles (arrowed) should be noted. The junction in the centre of the image is partially obscured by an out of focus thin lath of brown mica. Data for this sample are presented in Table 3. Scale bar is 200 µm long. (d) Sample 1Wl329.2 from UZc of the Bushveld Intrusion (plane-polarized light). The cumulus apatite (ap) and the high dihedral angle (arrowed) should be noted. Data for this sample are presented in Table 3. Scale bar is 200 µm long.

predominantly anhedral (Fig. 5b), and a reduction in the mode of interstitial phases (quartz is virtually absent, although biotite is commonly associated with Fe–Ti oxides; Fig. 5b). Late-stage mafic symplectites of the type ascribed to liquid immiscibility by Holness *et al.* (2011) grow from the oxides, replacing primocrystic plagioclase (Fig. 5b). The base of UZb is marked by the arrival of cumulus olivine and the gradual loss of orthopyroxene, and the base of UZc is defined by the first arrival of cumulus apatite. However, the presence of both olivine and apatite is cyclical (Cawthorn & Walsh, 1988; Tegner *et al.*, 2006). The geometry of augite–plagioclase–plagioclase three-grain junctions changes significantly, with low dihedral angles just above the Pyroxenite Marker (Fig. 5c) and wider junctions (high dihedral angle) at the top of Upper Zone (Fig. 5d).

Choice of samples

We measured Θ_{cpp} in selected samples through the three Bierkraal drill cores. The correlations between the three cores are those used by Kruger *et al.* (1987) and Tegner *et al.* (2006): 1600 m depth below the upper contact with the overlying granite in BK1 equals 550 m depth below the borehole collar in BK3, and 1420 m depth below the collar in BK3 equals 200 m depth below the collar in BK2. Cumulus magnetite appears at 1862 m, cumulus olivine appears at 1662 m, and the stratigraphically lowest arrival of cumulus apatite is at 1128 m below the overlying granite, marking the base of UZc. We measured between 48 and 100 three-grain junctions in each sample (using more than one thin-section if necessary) to obtain Θ_{cpp}. The results are given in Table 3.

The Sept Iles layered intrusion, Quebec
Geological setting

The Sept Iles layered intrusion is on the north shore of the St. Lawrence River, ~500 km to the NE of Quebec City. It is the third largest layered igneous body on Earth and was emplaced 564 ± 4 Myr ago (Higgins & van Breeman, 1998) at the unconformity between high-grade gneisses of the Grenville Province and overlying flood basalts (Higgins, 2005). It has an approximately circular plan, 80 km in diameter, with a maximum thickness of 5·5 km. Layering at the margins dips ~30° towards the centre of the intrusion, giving it an overall shape like a dinner plate. The intrusion has been divided into three: the Layered Series, the Upper Border series and the Upper Series (Cimon, 1998; Higgins, 2005; Namur *et al.*, 2010). The 4·7 km thick layered series is made of three megacyclic units (MCU) each resulting from the crystallization of a new influx of ferrobasaltic magma (Namur *et al.*, 2010, 2011). Up to six minor replenishment events occurred during the formation of Megacyclic Unit II (MCU-II), whereas the underlying 1785 m thick Megacyclic Unit I (MCU-I) solidified as a closed system.

Petrography

The cumulates from the lowest part of MCU-I contain cumulus plagioclase and olivine only, with interstitial augite, (Ca-poor) orthopyroxene, oxides, biotite, apatite and amphibole. Augite and the orthopyroxene form cuspate grains in plagioclase-rich areas, small oikocrysts, and rims around cumulus olivine (Fig. 6a). Augite is variably replaced by brown amphibole. Amphibole and biotite form isolated interstitial grains as well as rims around interstitial Fe–Ti oxide grains (Fig. 6a). Progressive fractionation leads to the saturation of the liquid with Fe–Ti oxides at a stratigraphic height of about −3700 m [using the scheme of Namur *et al.* (2010)]: these form abundant rounded grains. Here the interstitial amphibole (and, more rarely, biotite) generally forms rims around the cumulus oxide grains (Fig. 6b), rather than isolated grains. The mode of this rimming amphibole decreases up-section: it is uncommon (<2 vol. %) by about −3000 m stratigraphic height, and rare (≪1 vol. %) by about −2500 m. The biotite mode also decreases over the same interval.

The arrival of cumulus augite on the liquidus (at a stratigraphic height of about −3400 m) is marked by an increase in augite mode and grain size, with local replacement and overgrowth by brown amphibole (Fig. 6c). Interstitial orthopyroxene disappears once augite is cumulus. In the interval between −3000 and −2600 m, the modal proportion of olivine is commonly less than 5 wt %, indicating an intercumulus status for olivine in this interval (Namur *et al.*, 2010). This interpretation is supported by the tendency of many of the remaining olivine grains to grow as extensive rims around oxides (Fig. 6d). The absence of cumulus orthopyroxene in the region of the stratigraphy in which olivine is intercumulus suggests that there was no reactive relationship between the two phases, in contrast to that seen in the Skaergaard and Bushveld intrusions. The arrival of cumulus apatite (at −2580 m) is marked by an increase in mode and a change in morphology from subhedral to euhedral. The olivine mode also increases at this point and we consider it to have rejoined the cumulus assemblage (Namur *et al.*, 2010), although the stratigraphic position at which this occurs is difficult to determine precisely from olivine mode and morphology alone. We follow Namur *et al.* (2010) in placing the arrival of apatite and the return of olivine at −2580 m.

Although this pattern of changes in the cumulus assemblage is broadly similar to that of Skaergaard, there are two notable differences. The first is that the greater enrichment of the Sept Iles magma in Fe and Ti compared with Skaergaard resulted in the saturation of the MCU-I liquid in oxides before saturation in augite (Namur *et al.*, 2010). The second is that the disappearance of cumulus olivine is not associated with an increase in the mode of Ca-poor pyroxene. Late-stage symplectites of the type associated with liquid immiscibility are absent in MCU-I (Namur
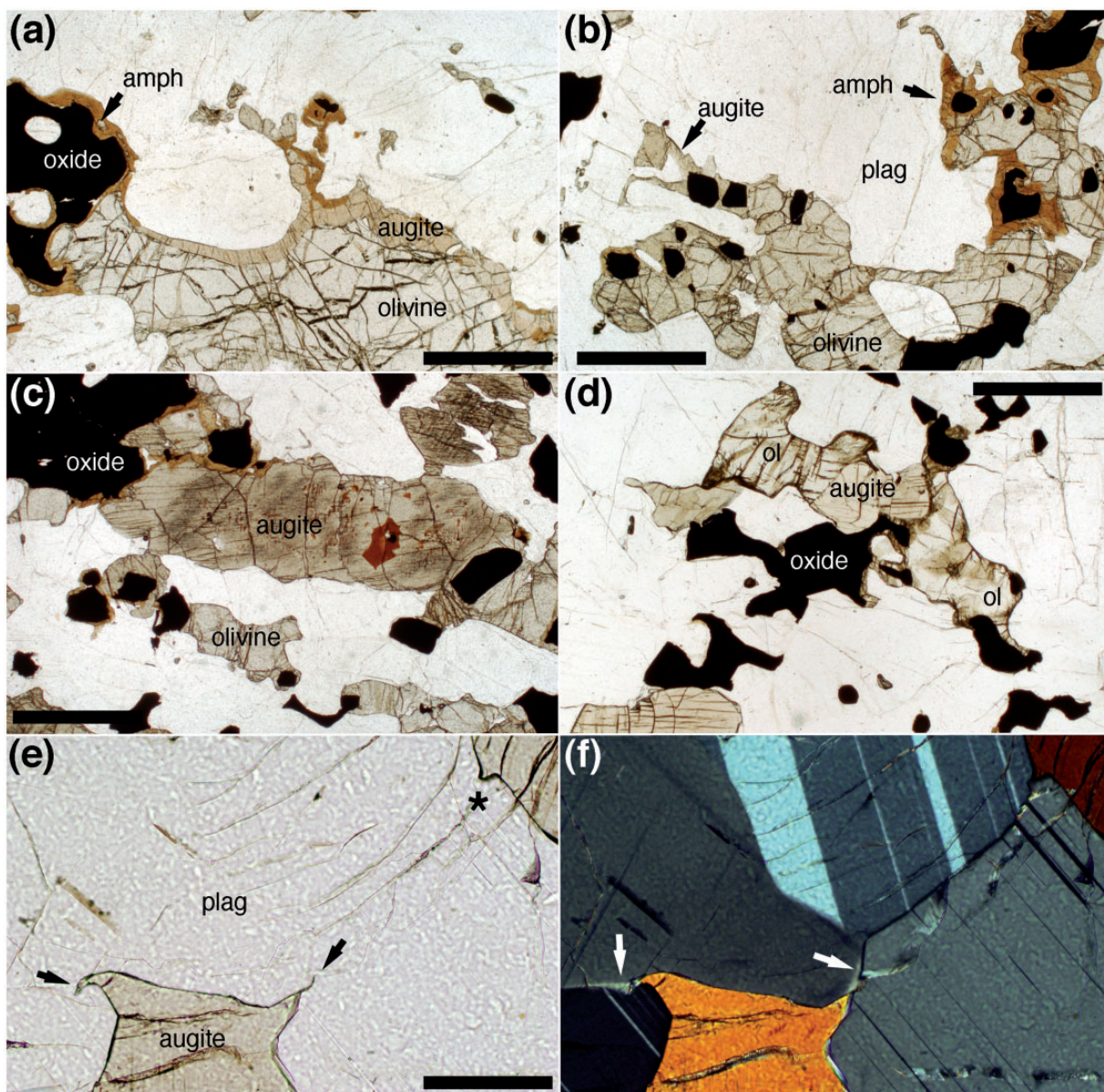
Fig. 6. Photomicrographs of microstructures in MCU-I of the Sept Iles layered intrusion [all in plane-polarized light, except (f)]. Data for each sample are presented in Table 4. (a) Sample DC9-2410.0. Augite forms interstitial cuspate grains and rims around olivine. There is local replacement or overgrowth of augite by brown amphibole, which also rims the interstitial oxides. Scale bar is 200 μm long. (b) Sample DC9-1874.5. Fe–Ti oxides are cumulus. Noteworthy features are the rim of augite on cumulus olivine and Fe–Ti oxide grains, and the monocrystalline rim of brown amphibole surrounding the cumulus grains in the top right corner of the image. Scale bar is 1 mm long. (c) Sample DC9-1514.5. Augite is now cumulus and forms large elongate grains, variably replaced by amphibole. Scale bar is 1 mm long. (d) Sample DC9-740.5. Olivine is not cumulus in this sample, with a low mode. The extensive rims extending from the olivines and surrounding the cumulus Fe–Ti oxide grains should be noted. Scale bar is 1 mm long. (e, f) Sample DC9-740.5. Many augite–plagioclase–plagioclase three-grain junctions in this sample have developed fish-hook augites [arrowed in (e)] associated with deflection of the original plagioclase–plagioclase grain boundary and the growth of Ca-rich plagioclase [arrowed in (f)]. These features are caused by late-stage reactive fluids (Holness *et al.*, 2011), but the fluids are not entirely pervasive as some junctions remain unaffected [marked by an asterisk in (e)]. Scale bar is 200 μm long in both images.

et al., 2012). Between about −2740 m and −2539 m cumulus augite grains locally develop fish-hook extensions along plagioclase–plagioclase grain boundaries, associated with plagioclase reverse zoning (Fig. 6e and f). Features of this type have been attributed to the presence of late-stage

reactive liquids (Holness *et al.*, 2011) and they are therefore unlikely to be primary microstructures formed during the main phase of solidification. Three-grain junctions involving fish-hook extensions were not included in the dihedral angle populations.

Choice of samples

Much of the intrusion is unexposed, although a nearly complete traverse through the stratigraphy is available as drill core. We examined a suite of samples through MCU-I from the drill core BH84699, kept at the Ministère des Ressources Naturelles et de la Faune du Québec. The choice of samples from the lower part of the stratigraphy, in which augite is interstitial, was confined to those containing sufficient augite [modal proportions for all the samples have been reported by Namur & Charlier (2012)] to permit at least 25 measurements per thin-section (with two thin-sections for each sample). We measured the orthopyroxene–plagioclase–plagioclase dihedral angle in sample DC9-1855.0.

RESULTS

The new values of Θ_{cpp} obtained for the Rum allivalites (Table 1) are very similar to those already presented by Holness *et al.* (2007*a*, 2007*b*) and Holness & Winpenny (2009), differing by only a few degrees and well within the 2σ confidence interval. This reinforces the conclusion of Riegger & van Vlack (1960) that a good first-order approximation of Θ_{cpp} can be obtained from populations of only 30 measurements. Values for the troctolitic allivalite are generally ~80° except for samples collected immediately below minor peridotite horizons: these have higher angles. Θ_{cpp} for the gabbroic allivalites are ~90°, confirming the bimodal distribution of median angles previously described. Standard deviations of these populations are
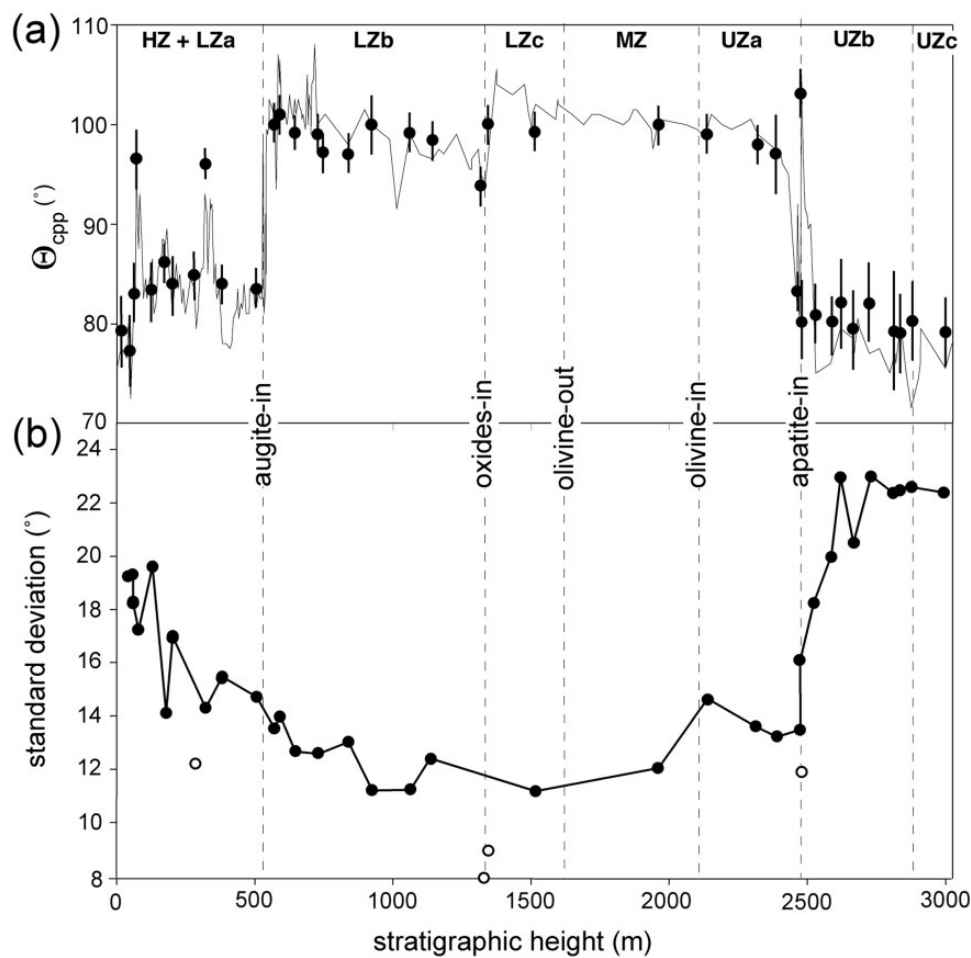
Fig. 7. (a) Median augite–plagioclase–plagioclase dihedral angle, Θ_{cpp}, as a function of stratigraphic height for the Skaergaard Layered Series. The zero point of the stratigraphy is taken as the base of the Cambridge drill core. The dots show Θ_{cpp} determined as part of this study, with 95% confidence intervals calculated according to Stickels & Hücke (1964). It should be noted that the error bars are longer for samples with low Θ_{cpp}, reflecting the greater spread of angles in these samples. The continuous line shows the results of Holness *et al.* (2007*a*). (b) The stratigraphic variation of standard deviation of dihedral angle. Black dots denote samples for which 100 measurements were made, and the open circles are data for samples with smaller populations—the standard deviation for the latter is likely to be incorrect. The slow decline of standard deviation from the base of the intrusion upwards through LZb should be noted (with no deflection at the LZa–b boundary, despite the large stepwise increase in median angle). Low standard deviation continues through LZc, MZ and UZa until a major increase in UZb corresponding to the absence of curvature of augite–plagioclase boundaries (Fig. 3f and h).

generally higher for samples with low Θ_{cpp}, and the skew of the populations is generally negative (i.e. with a longer tail towards the lower end of the distribution).

A direct comparison of the previously published Θ_{cpp} for the Skaergaard Layered Series and the new values obtained from much larger populations is shown in Fig. 7a. There is excellent correspondence between the old and new sets of data, although samples with low Θ_{cpp} may differ by up to $5°$. It should be noted that the high variability of Θ_{cpp} previously reported for UZb and UZc is most probably due to the smaller populations used in the earlier work; with the larger populations of this study Θ_{cpp} remains within a much narrower range. The first-order stratigraphic variation of Θ_{cpp} in the Skaergaard intrusion is the stepwise increase at the arrival of a new liquidus phase (i.e. at the bases of LZb, LZc and UZb). There is no change at either base or top of MZ, suggesting that the reaction relationship between liquid, olivine and orthopyroxene has no effect on Θ_{cpp}. The localized positive excursions in Θ_{cpp} previously reported in the HZ (Holness et al., 2007a) are well defined and will be discussed in a later contribution.

Towards the top of UZa, Θ_{cpp} abruptly declines to $\sim83°$, apart from a local positive excursion related to the arrival of cumulus apatite (Fig. 7a). The decline is associated with the development of planar augite–plagioclase grain boundaries, and a change in morphology of interstitial apatite from euhedral to anhedral (Figs 3f, h and 4d). The increase in Θ_{cpp} associated with the saturation of the bulk

liquid in apatite (and a consequent morphological change of apatite from anhedral back to euhedral) is a result of the reintroduction of curved augite–plagioclase grain boundaries at three-grain junctions. However, after a stratigraphic interval of $\sim35\,m$ the curvature disappears and Θ_{cpp} decreases again. This transition to microstructures locally reminiscent of those seen in rapidly cooled dolerites is not seen in the other intrusions examined here.

Standard deviation decreases slowly through HZ and LZb, reaching low constant values of $\sim12°$ through much of the stratigraphy (Table 2, Fig. 7b). The development of planar augite–plagioclase grain boundaries is associated with an abrupt increase of standard deviation to $\sim22°$, reflecting the influence of the original impingement angle of the plagioclase grains on the final dihedral angle. It should be noted that the major stepwise increase in Θ_{cpp} associated with the arrival of cumulus augite is not reflected in the standard deviation, which smoothly declines through this boundary. The skew of the angle populations for Skaergaard cumulates is almost always negative (Table 2).

The stratigraphic variation of Θ_{cpp} in the Bushveld Complex is shown in Fig. 8. Θ_{cpp} remains constant over large stretches of stratigraphy, increasing in a stepwise fashion both at the arrival of cumulus oxides and and at the arrival of apatite. The magnitude of the steps ($\sim5°$) is smaller that some of those seen in the Skaergaard (compare augite-in and apatite-in), but they are greater than the 95% confidence intervals. In common with the
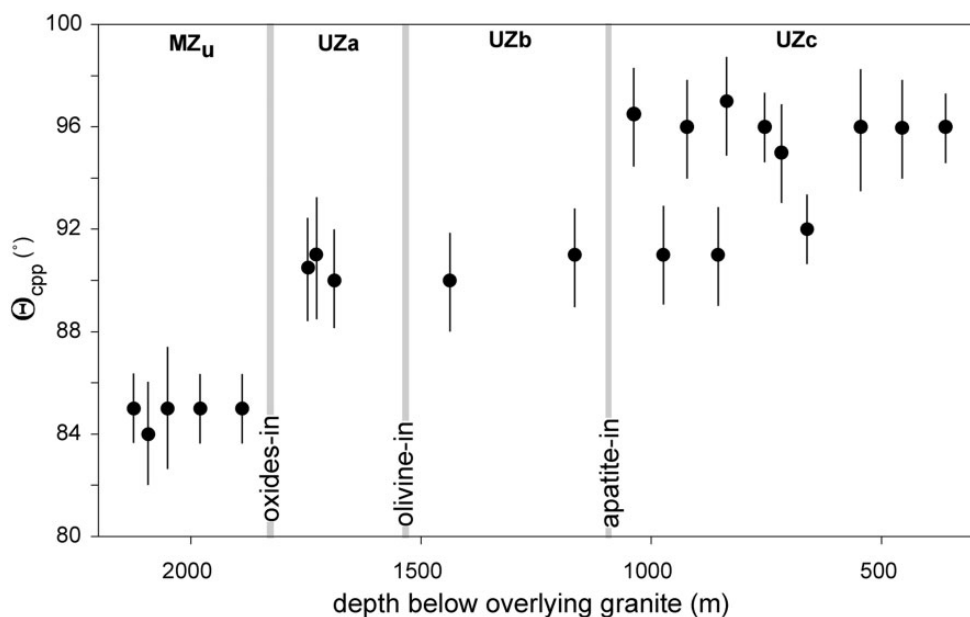
Fig. 8. Stratigraphic variation of Θ_{cpp} in the upper part of the Bushveld Intrusion as sampled by the Bierkraal drill cores. The error bars are the 95% confidence intervals calculated according to Stickels & Hücke (1964). The base of UZa is marked by the arrival of cumulus Fe–Ti oxides, the base of UZb is marked by the arrival of cumulus olivine and the base of UZc is marked by the arrival of cumulus apatite. The bimodal variation of Θ_{cpp} in UZc should be noted.

Skaergaard rocks, there is no change of Θ_{cpp} associated with the arrival of cumulus olivine and the associated disappearance of orthopyroxene. Θ_{cpp} in UZc is bimodal, with some rocks having angles indistinguishable from those of UZb whereas others are up to 6° higher. This bimodality is reflected in the bulk-rock P_2O_5 content (Fig. 9), with the samples with high Θ_{cpp} generally containing more P_2O_5 than those with low Θ_{cpp} (the single exception is sample 1W 908.6, which contains very little apatite but has a high Θ_{cpp}). The bimodality therefore is most probably related to whether or not apatite is a cumulus phase in the UZc cumulates (see Tegner *et al.*, 2006), consistent with the higher Θ_{cpp} being associated with the arrival of cumulus apatite.
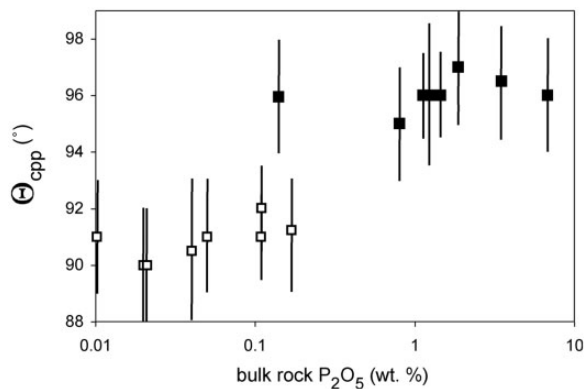
Fig. 9. The variation of Θ_{cpp} with the bulk-rock P_2O_5 content in the upper part of the Bushveld Intrusion (from Tegner *et al.*, 2006). The open squares are data for UZa and UZb samples (for which apatite is an interstitial phase); the filled squares are data for UZc (in which apatite is locally cumulus). The samples divide into two groups, one with low Θ_{cpp} and low bulk-rock P_2O_5, and the other with high Θ_{cpp} and high P_2O_5.

The stratigraphic variation of Θ_{cpp} in MCU-I of the Sept Iles intrusion is shown in Fig. 10. Again Θ_{cpp} remains constant through large stretches of the stratigraphy, with stepwise increases associated with the arrivals of cumulus oxides and augite. These two steps are ~10° high, well outside the 95% confidence intervals. The median orthopyroxene (h)–plagioclase–plagioclase dihedral angle in sample DC9-1855.0 in Sept Iles MCU-1 (Θ_{hpp}) is indistinguishable from Θ_{cpp} in other samples containing the same liquidus assemblage, consistent with the observations of Holness *et al.* (2012b), who found $\Theta_{hpp} = \Theta_{cpp}$ in dolerites of the Basement Sill, Antarctica. The loss of cumulus olivine is marked by a decrease in Θ_{cpp}. This is followed by an increase associated with the arrival of cumulus apatite and the return of olivine. These two uppermost stepwise changes are small but significant relative to the 95% confidence intervals on Θ_{cpp}. The sample immediately below the position of apatite/olivine-in (sample number DC9-559) has a relatively high dihedral angle. The position of olivine-in is not well defined in the sample suite (although that of apatite-in is easily discernible) and it is possible that the actual position of olivine-in lies below sample DC9-559 (see fig. 2 of Namur & Charlier, 2012).

The relationship between Θ_{cpp} and standard deviation for the Skaergaard, Rum and some Bushveld samples is shown in Fig. 11 (the angle populations for the Sept Iles and the other Bushveld samples are too small to justify discussion of any variation of standard deviation). All data points fall between plagioclase–plagioclase–melt impingement angles (data from Holness *et al.*, 2012a) and sub-solidus augite–plagioclase–plagioclase equilibrium (Holness *et al.*, 2012a), in common with data points for the Portal Peak dolerite sill (from Holness *et al.*, 2012b). The data for Skaergaard LZb, LZc and MZ fall between sub-solidus
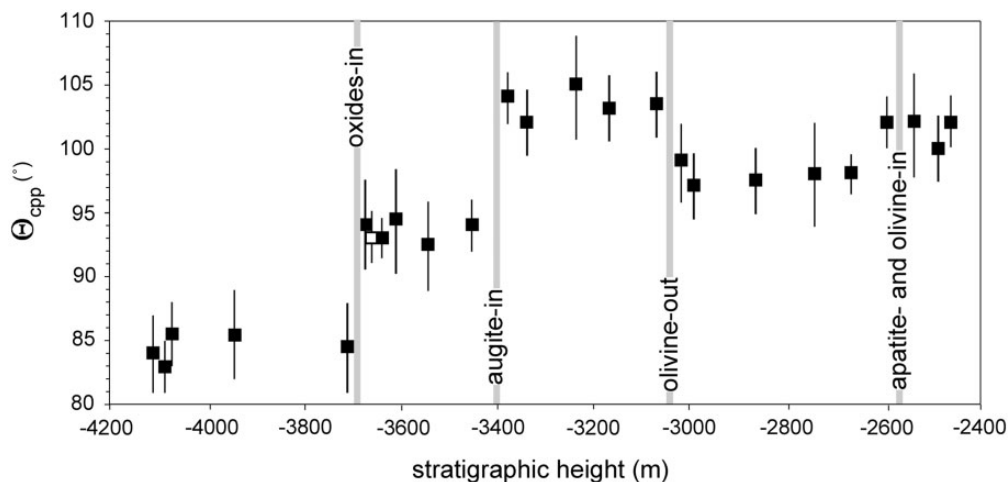
Fig. 10. Stratigraphic variation of Θ_{cpp} in MCU-I of the Sept Iles intrusion. The error bars are the 95% confidence intervals calculated according to Stickels & Hücke (1964). The arrivals of cumulus oxides and augite are marked; the reverse order compared with Bushveld and Skaergaard should be noted. The open square is for sample DC9-1855.0, for which orthopyroxene–plagioclase–plagioclase angles were measured. The value of Θ_{hpp} is indistinguishable from Θ_{cpp} of nearby samples.
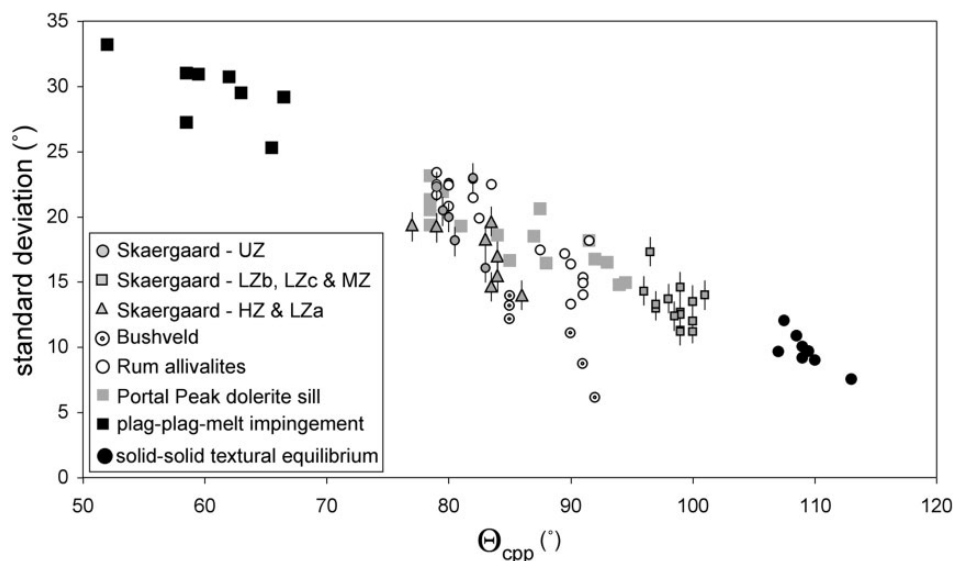
Fig. 11. The variation of Θ_{cpp} with standard deviation for several suites of samples. Only those for which we collected ~100 measurements are shown, because the standard deviation is not well constrained for smaller populations. The error bars for Θ_{cpp} are not shown, and indicative uncertainties of $\pm1°$ on the standard deviation are shown only for the Skaergaard data: the errors on the other data points are similar but are not shown for clarity. The plagioclase–plagioclase–melt impingement and the sub-solidus textural equilibrium data are from Holness *et al.* (2012*a*), whereas the Portal Peak data are from Holness *et al.* (2012*b*).

textural equilibrium and the data from the central parts of the Portal Peak sill, but there are two distinct populations of low Θ_{cpp} samples. The samples from UZc of Skaergaard (i.e. those with three-grain junctions formed by the meeting of planar augite–plagioclase grain boundaries) are indistinguishable from those of the rapidly cooled marginal regions of dolerite dykes, whereas those of HZ and LZa generally have lower standard deviations than the Portal Peak dolerite samples. The standard deviations for the Bushveld samples and some of the Rum gabbroic allivalites are also lower than those of the dolerite.

DISCUSSION

The major feature of the three layered intrusions for which we have data from a continuous sequence of progressively more evolved cumulates is that Θ_{cpp} generally remains constant over long vertical successions with constant mineralogy (with the exceptions of a 5° decline through LZb, and the major drop in Θ_{cpp} in UZb in the Skaergaard intrusion) with statistically significant stepwise changes corresponding to a change in the number of phases on the liquidus of the bulk magma. A similar behaviour is inferred for the Rum allivalites, although this intrusion does not have a clear continuous sequence of progressive fractionation. This pattern of Θ_{cpp} variation is very different from that in unfractionated mafic intrusions such as sills in which the dihedral angle is a smooth function of position within the sill (Fig. 2).

What controls Θ_{cpp} in layered intrusions?

Holness *et al.* (2012*b*) showed that Θ_{cpp} in dolerite sills is a sensitive function of the time taken to solidify, via the primary control of relative crystal growth rates in determining the geometry of pyroxene–plagioclase–plagioclase junctions. Here we suggest that the rate of growth of plagioclase compared with augite is also a contributory control on Θ_{cpp} in layered intrusions. This is supported by the commonly observed asymmetry of three-grain junctions, for which the junction geometry appears to be linked to the orientation of the (010) growth face of one of the plagioclase grains involved (Fig. 3b and d).

The schematic illustration in the bottom panel of Fig. 12a shows the most commonly observed geometry, with the outwards-convex surface of the augite adjacent to that plagioclase grain (grain A) whose (010) face defines the orientation of the plagioclase grain boundary (see Figs 1e, f and 3d). Curved inter-phase boundaries are generated by simultaneous growth of the two minerals if their interfaces with the remaining melt are at different orientations and if the growth rates are different. That the boundary between grain A and the augite far from the three-grain junction is parallel to the plagioclase (010) plane suggests that, initially, augite grew much faster than grain A. But as solidification continued, the growth rate of grain A became faster than that of the augite. Conversely, the curvature of the boundary between the augite and grain B points to augite growing faster than the plagioclase as the three-grain junction is formed. For simplicity, in Fig. 12a the two interphase boundaries are shown
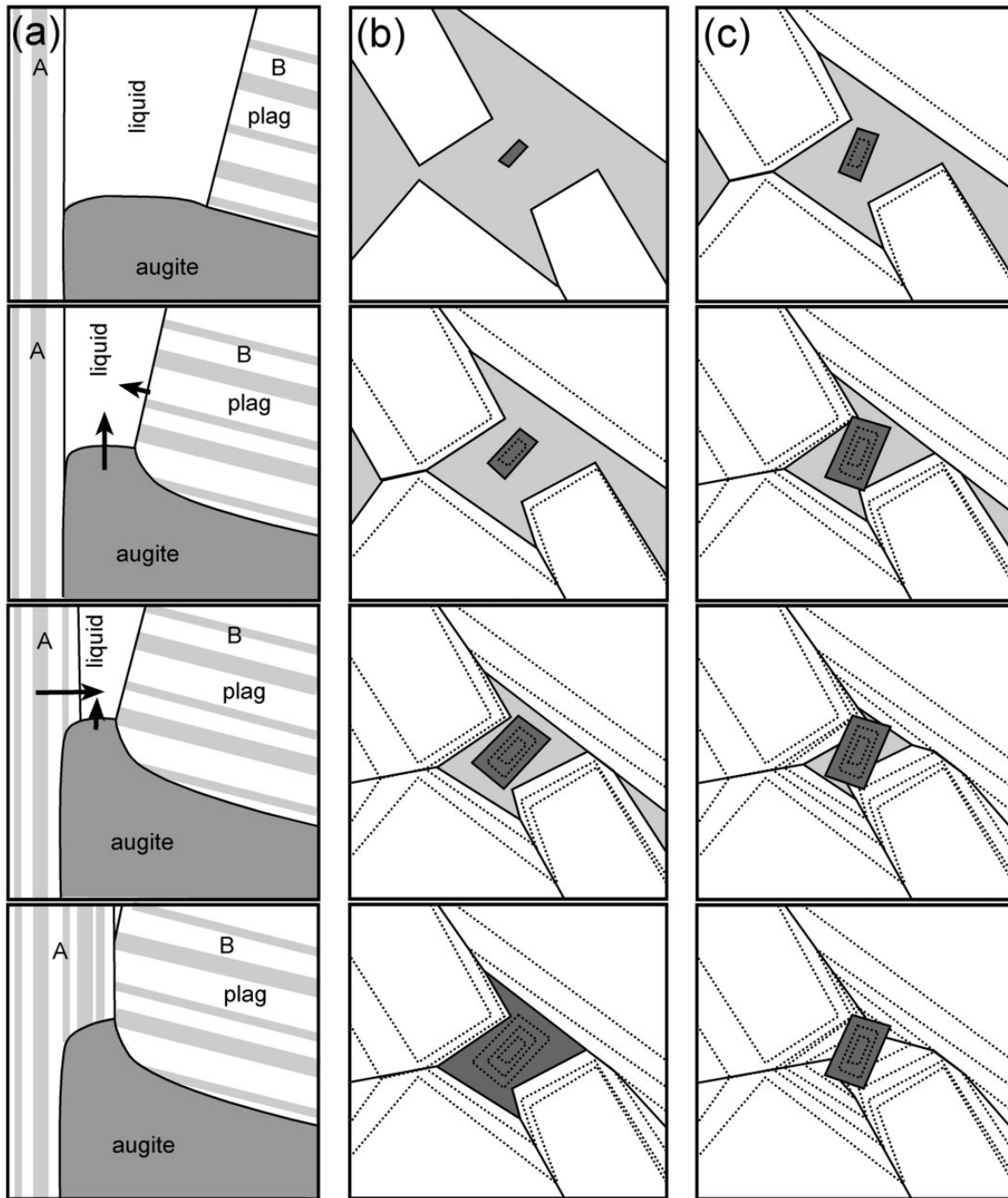
Fig. 12. Schematic illustrations showing the development of three-grain junctions. (a) A simplified and schematic model for the formation of an augite–plagioclase–plagioclase junction. The arrows denote grain growth and the relative lengths of the arrows denote relative growth rates. In the top panel an augite grain has grown into the liquid-filled space between two plagioclase grains. Curvature of the junction between plagioclase B and the augite is created during the simultaneous growth of the two grains because augite growth is faster than that of grain B (second panel). During the last stage of solidification, plagioclase grain A begins to grow rapidly, filling most of the remaining pore space and creating curvature of the resultant plagioclase–augite grain boundary (third panel). This pattern of relative growth rates of the three grains leads to the commonly observed asymmetry of the three-grain junction (bottom panel). The faster the relative growth of grain A during this last stage, the higher the resultant value of the dihedral angle. (b) Growth of apatite in a plagioclase-bounded pore. The first three panels show simultaneous growth of faceted apatite and plagioclase grains. If the plagioclase ceases to grow during the last stages of solidification, the apatite grows to fill the remaining space, creating an anhedral grain with a shape determined by the faceted plagioclase walls (bottom panel). (c) Growth of apatite in a plagioclase-bounded pore in which the plagioclase and apatite grow simultaneously throughout. In this case the apatite remains euhedral, and the apatite–plagioclase–plagioclase three-grain junctions are defined by impingement of the three grains.

developing separately, but it is likely that growth on all three grains was simultaneous during the last stage of solidification. Importantly, the faster and more pronounced the late growth of the (010) face of grain A compared with that of augite, the higher the resultant dihedral angle (bottom two panels in Fig. 12a).

Further evidence that the plagioclase growth rate plays a dominant role in controlling Θ_{cpp} is provided not only by the observation that the composition and structure of the pyroxene appear to be immaterial to three-grain junction geometry (i.e. $\Theta_{hpp} = \Theta_{cpp}$), but also by the complex stratigraphic sequence of microstructural evolution in the Skaergaard UZ. The stratigraphically lowermost changes in the microstructure are the reduction in curvature of augite–plagioclase junctions (Fig. 3f–h) and the associated transition from euhedral to anhedral interstitial apatite (Fig. 4) that occur through UZa. These two changes correlate with a gradual reduction of Θ_{cpp}. Θ_{cpp} then increases markedly as the bulk liquid saturates with apatite: the cumulates above this level are rich in euhedral apatite. The cumulates in the UZ also record a transition in the behaviour of the interstitial liquid, which, at this level in the Layered Series, comprises two conjugate immiscible components (Holness et al., 2010). The UZa cumulates contain late-stage reactive symplectites (Fig. 3e; attributed to the loss of the silica-rich conjugate liquid from the mushy layer) whereas the overlying UZb cumulates contain coexisting pockets of granophyre (Fig. 3g and h) and ilmenite-rich intergrowths [not illustrated; attributed to the retention of the silica-rich conjugate (Holness et al., 2010)]. This transition occurs over some tens of metres of stratigraphy.

Planar augite–plagioclase grain boundaries denote a relatively high rate of augite growth compared with the growth of plagioclase. The augite is essentially growing into a passive pore-space. We can deduce that the change in relative growth rates is due to a slowing of the plagioclase growth rate, rather than an increase in augite growth rate, because of the accompanying morphological change in the interstitial apatite. Three-grain junctions between euhedral apatite and plagioclase are commonly formed by the random intersection of plagioclase grain boundaries with apatite growth facets—it is likely that melt was expelled from the melt-filled pores by the simultaneous growth of faceted grains of apatite and plagioclase that subsequently impinge (Fig. 12c). In contrast, anhedral apatite is most probably formed by growth into melt-filled pores bounded by essentially passive (i.e. non-growing or very slowly growing) faceted plagioclase grains (Fig. 12b). These microstructures, together with the low Θ_{cpp}, are therefore caused by a cessation (or significant slowing) of growth of plagioclase during the last few per cent of solidification (i.e. in the lowermost parts of the crystal mush layer).

The reason for the reduction in plagioclase growth rate in the lowest levels of the mush in the Skaergaard UZb cumulates cannot be a result of changes in the interstitial liquid, because the association of low Θ_{cpp}, anhedral apatite and planar augite–plagioclase grain boundaries occurs both in rocks containing symplectites and in those with the paired late-stage intergrowths. The absolute plagioclase growth rate, and its growth rate relative to augite (and apatite), both in the Skaergaard UZ and throughout the rest of the Skaergaard Layered Series (and, by extension, in all four intrusions studied here) must therefore be controlled by a parameter external to the mush.

This external control in non-fractionating dolerite sills is the cooling rate. The dolerite data presented by Holness et al. (2012b) demonstrate that Θ_{cpp} is ~78° for magma solidified in fewer than ~10 years, rising to 100° for solidification times of 450 years. The range of Θ_{cpp} observed by Holness et al. (2012b) almost covers the range of angles seen in the four layered intrusions described here. However, we are not confident that the scaling between Θ_{cpp} and cooling rate developed for sills (Holness et al., 2012b) can be directly applied to fractionating systems because there are major differences between the uniform composition of the solidification fronts operating in sills and the fractionating mushy layers of larger intrusions.

Clues as to why and how three-grain junction formation in fractionated magma bodies is not exactly analogous to that in dolerites may be present in the variation of standard deviation through the Skaergaard Layered Series (Fig. 7b). The smooth change of standard deviation across the large Θ_{cpp} step at augite-in suggests that the details of the formation of three-grain junctions at this level in the intrusion are independent of the actual angle at which the two plagioclase grains meet, and result in a relatively narrow range of dihedral angles (and low standard deviation). Comparatively low standard deviations are also typical of other layered intrusions (e.g. the Bushveld Upper Zone, Fig. 11), consistent with some process of three-grain junction formation that is independent of the actual angle at which the two plagioclase grains meet.

Whatever drives and controls the process by which three-grain junctions form changes significantly in the Skaergaard UZ. Here the standard deviation increases, owing to the importance assumed by the original, random impingement of the plagioclase grains on the morphology of the junction following the cessation of plagioclase growth during junction formation. This change is not observed in the other intrusions, most probably because we did not consider the extremely fractionated parts of these intrusions.

Given these significant deviations from the behaviour observed in non-fractionated sills, we cannot yet interpret Θ_{cpp} in terms of crystallization time-scales in layered

intrusions. We will address this problem in a forthcoming contribution.

What is causing the steps?

The stepwise changes in Θ_{cpp} can be understood from several key deductions that can be made from the data presented here. Perhaps the most significant observation concerns the behaviour of Θ_{cpp} in response to the loss and gain of cumulus olivine. In both Skaergaard and Bushveld, in which a reaction relationship between olivine, low-Ca pyroxene and liquid has been inferred, there is no change in Θ_{cpp} associated with the loss of olivine. In contrast, Sept Iles cumulates at the levels where olivine disappears from the liquidus assemblage do not contain low-Ca pyroxene and there cannot be a similar reaction relationship: here we see a reduction in Θ_{cpp} when olivine disappears, followed by an increase when olivine (in association with apatite) reappears. We can deduce from this that it is the addition or subtraction of a phase from the liquidus assemblage that is responsible for the stepwise changes. The replacement of one phase by another (e.g. the interchange of olivine and low-Ca pyroxene) does not affect Θ_{cpp}.

The next question concerns the importance of composition, both of the cumulus phase being added or removed from the liquidus assemblage and of the interstitial liquid. Our data show that the stepwise changes occur regardless of the details of the liquid line of descent. Skaergaard residual liquids become progressively more Fe-rich after magnetite saturation, whereas the Bushveld and Sept Iles liquids became relatively Fe-depleted after oxide saturation (Tegner & Cawthorn, 2010; Namur *et al.*, 2011). Stepwise increases occur in Sept Iles at the arrivals of cumulus oxides and augite, even though the order of arrival is the reverse of that seen in Bushveld and Skaergaard. The composition of the new cumulus phase is clearly immaterial.

What role does the interstitial liquid play in forming the steps? The remaining interstitial liquid provides the pathway for the movement of the elements required to form pyroxene and plagioclase towards the nascent three-grain junction and the removal of rejected elements. Solidification and fractionation causes the composition of this interstitial liquid to vary continuously, with no discontinuous stepwise changes. It is therefore unlikely that Θ_{cpp} is governed by compositionally controlled stepwise changes in mass transport rates. Furthermore, the observed differences in both interstitial mineral assemblages and the amounts of interstitial liquid present in the four intrusions demonstrate that neither the composition of this liquid nor its volumetric amount can be playing a role in determining the existence of the stepwise changes in Θ_{cpp}. Composition, of either the interstitial liquid or the cumulus assemblage, is therefore not the controlling factor determining the pattern of Θ_{cpp} stratigraphic variation in layered intrusions. It is entirely possible, however, that

whereas composition cannot control the existence of the stepwise changes, there might be a secondary compositional effect modifying step magnitude.

We also discount the role of metasomatism in creating the stepwise changes in Θ_{cpp} (see McBirney *et al.*, 2009). We find it highly implausible that four separate layered intrusions would have undergone pervasive, but previously undocumented, metasomatism resulting in discrete changes to the geometry of three-grain junctions precisely at the stratigraphic horizons at which liquidus phases appear or disappear.

The only remaining hypotheses to account for the coincidence of changes in three-grain geometry with changes in the liquidus assemblage concern changes in physical parameters.

The enthalpy budget of a fractionating system

The general pattern of stratigraphic variation of Θ_{cpp} points to relatively constant physical conditions for large stretches of stratigraphy, followed by stepwise changes that result in an change of plagioclase growth rate relative to augite (we neglect Skaergaard UZ in this analysis—we will return to the reason why plagioclase ceases to grow at the base of the mush in these cumulates in a later contribution). The enthalpy budget of a fractionating system undergoes stepwise changes associated with changes in the liquidus assemblage.

Ghiorso (1997) has documented how the amount of crystallization for each increment of cooling—the crystal productivity of Morse (2011)—increases abruptly as a new phase is added to the liquidus assemblage before subsequently decaying. This is associated with a stepwise increase in the contribution of latent heat of fusion to the total enthalpy budget—the fractional latent heat of Holness *et al.* (2007*a*, 2009) and Morse (2011). We suggest that it is this that results in the stepwise changes in Θ_{cpp}. This can be illustrated by simple calculations of the enthalpy budget of a fractionating basaltic liquid.

We used the simplified CMASF (CaO–MgO–Al$_2$O$_3$–SiO$_2$–FeO) system, basing our choice of liquids on experimental data from Longhi (1987) and Shi & Libourel (1991) to ensure starting compositions within the olivine stability field (Table 5). To obtain contrasted sequences of crystallization, we chose one composition (CMASF-1) close to the olivine–anorthite cotectic curve, and another (CMASF-2) close to the peritectic reaction involving forsterite and protoenstatite. We also chose a more realistic 10-component starting composition similar to that of Nielsen (2004) that might mimic the behaviour of the Skaergaard magma (Table 5).

We used the MELTS/pMELTS thermodynamic calculator (Ghiorso & Sack, 1995; Ghiorso *et al.*, 2002). Calculations were performed at a pressure of 1 atm, under oxygen fugacity conditions buffered to the FMQ

Table 5: Results of calculations for the enthalpy budget for a range of synthetic and natural liquid compositions

	CMASF-1	CMASF-2	Skaergaard-like
SiO_2	46·94	51·94	48·86
TiO_2	–	–	2·04
Al_2O_3	14·98	11·99	14·25
FeO	7·89	8·87	13·1
Fe_2O_3	1·22	1·24	2·41
MnO	–	–	0·24
MgO	19·98	19·98	6·11
CaO	8·99	5·99	10·18
Na_2O	–	–	2·04
K_2O	–	–	1·02
Ratio of $\Delta H/\Delta T$ *before and after the step-change*			
	+plag = 21·3	+ opx = 3·6	+ cpx = 3·2
	ol → opx = 1·5	+ plag = 24·0	ol → opx = 1·17
	opx → cpx = 1·2	– ol = 0·5	+ mt = 5·9
	+cpx = 8·8		

The oxide contents of each starting liquid composition are given in wt %. The ratio of H/T before and after the step-change associated with the change in liquidus assemblage is calculated using the highest H/T following the change and the lowest H/T immediately preceding the change.

(fayalite–magnetite–quartz) buffer from the liquidus temperature to 1100°C, with a decrement of 1°C, assuming fractional crystallization. We assessed the accuracy of MELTS/pMELTS in predicting phase equilibria in the CMAS and CMASF systems by comparing the results of >50 calculations (liquidus temperature and predicted liquidus phases) with the experimental results of Presnall *et al.* (1979), Longhi (1987), Libourel *et al.* (1989) and Shi & Libourel (1991). Calculated liquidus temperatures are within 50°C of the experimental values, and the liquidus assemblage is accurately predicted, with the exceptions of quartz and spinel.

The crystallization of liquid CMASF-1 is characterized by the following sequence: olivine, olivine + plagioclase, orthopyroxene + plagioclase, clinopyroxene + plagioclase, orthopyroxene + clinopyroxene + plagioclase. The reactions involving the replacement of olivine by protoenstatite, and protoenstatite by diopside through pigeonite, have been described by Longhi (1987). During progressive fractionation, CMASF-1 becomes enriched in SiO_2 (from 45·9 to 53·2 wt %), CaO (9·0–9·6 wt %) and FeO_t (9·1–17·0 wt %), and depleted in MgO (from 20·0 to 3·5 wt %) and Al_2O_3 (15·0–11·2 wt %).

Crystallization of liquid CMASF-2 is characterized by the following sequence: olivine, olivine + orthopyroxene, olivine + orthopyroxene + plagioclase, orthopyroxene +

plagioclase. The disappearance of olivine is most probably related to the high silica activity of the melt after 80% of fractionation (Shi & Libourel, 1991). During fractionation CMASF-2 becomes enriched in SiO_2 (51·9–61·7 wt %) and Al_2O_3 (12·0–26·6 wt %) and depleted in CaO (6·0–4·1 wt %), FeO_t (10·1–3·9 wt %) and MgO (20·0–3·7 wt %).

The Skaergaard starting composition progressively crystallizes plagioclase + olivine, plagioclase + olivine + clinopyroxene, plagioclase + orthopyroxene + clinopyroxene, plagioclase + orthopyroxene + clinopyroxene + Fe–Ti oxides. This sequence is similar to that observed in the Skaergaard intrusion itself, although we did not continue the calculations further than $F = 0·37$ because the results are unlikely to be realistic. With differentiation, this liquid follows a trend of FeO_t enrichment at constant SiO_2 content until it becomes saturated in Fe–Ti oxides. After this point it follows a trend of strong SiO_2 enrichment and FeO depletion. The calculated liquid line of descent is therefore similar to that obtained experimentally by Toplis & Carroll (1995) and observed in ferrobasaltic provinces worldwide (Charlier *et al.*, 2013).

We calculated the enthalpy of the liquid at each increment of temperature and used this to calculate the change in enthalpy for each incremental change in temperature ($\Delta H/\Delta T$, where $\Delta T = 1°C$). Following Ghiorso (1997) we normalized the result using the mass of remaining magma in the system (F) so that we could assess the potential effect on the cooling rate of the magma body. Adjusting our values of $\Delta H/\Delta T$ by eliminating the contribution required to cool the system (i.e. by calculating the actual values of ΔH_{fus}) is not expected to change the results presented here.

The temperature derivative of ΔH generally decreases with F at a rate dependent on the stable liquidus assemblage (Fig. 13). This trend is punctuated by significant changes in $\Delta H/\Delta T$ associated with the appearance or disappearance of a new liquidus phase. The appearance of a new phase on the liquidus produces a significant jump (by a factor ranging from 3·2 to 21·3; Table 5) in $\Delta H/\Delta T$, whereas the single example of a disappearance of a liquidus phase (olivine in CMASF-2; Fig. 13b, Table 5) results in a halving of $\Delta H/\Delta T$. When a cumulus phase is replaced by another cumulus phase (e.g. olivine replaced by orthopyroxene, or orthopyroxene replaced by clinopyroxene in CMASF-1), $\Delta H/\Delta T$ undergoes no significant change (Table 5, Fig. 13a–c).

These calculations are consistent with a model in which the physical process resulting in the observed stepwise changes in Θ_{cpp} is the change in the enthalpy budget (i.e. a step change in the fractional latent heat and in the rate of change of total enthalpy with temperature) consequent to the increase or reduction of the number of phases on the liquidus of the bulk magma.
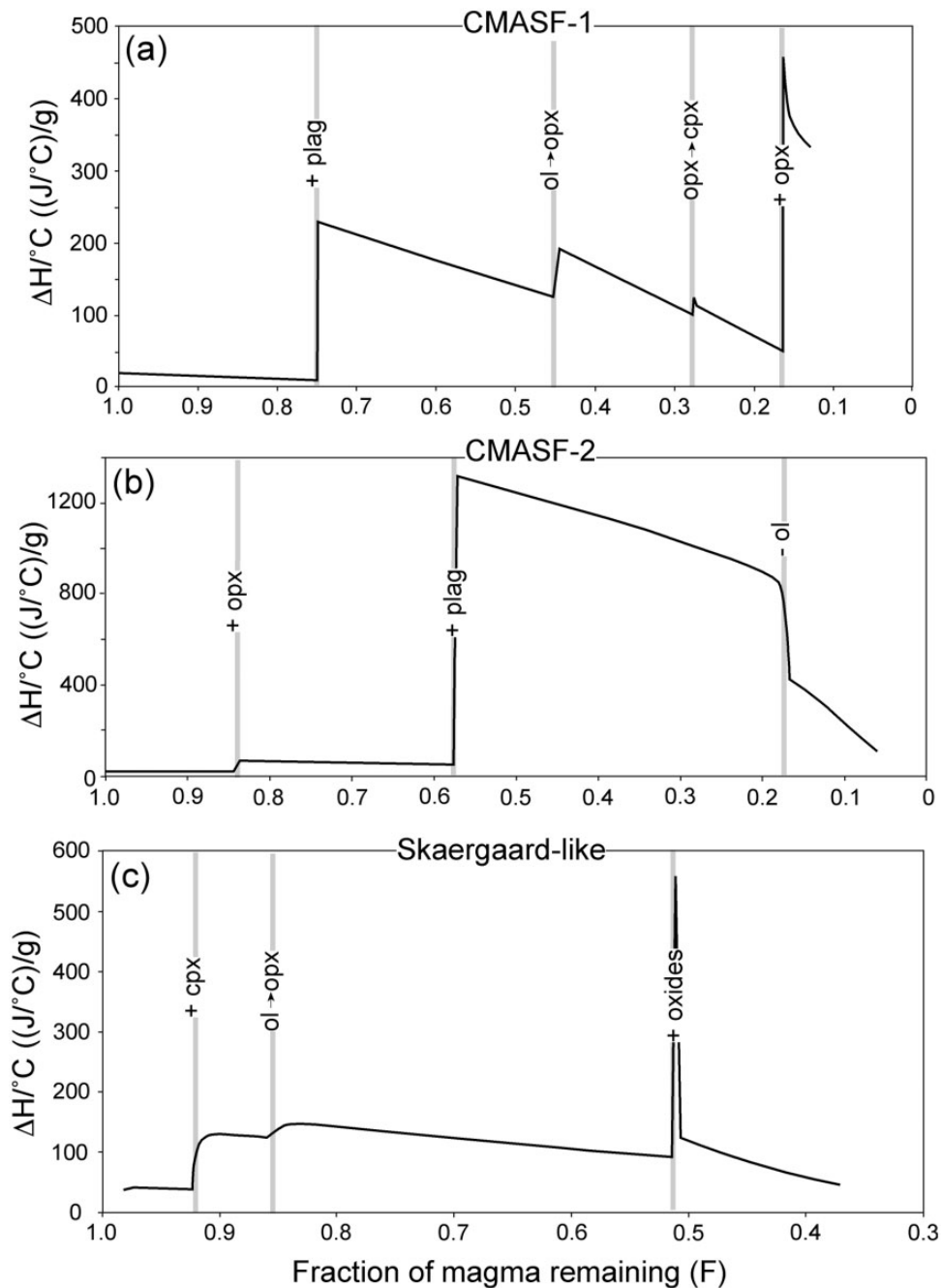
Fig. 13. The variation of $\Delta H/\Delta T$ normalised to the mass of remaining magma during progressive fractionation of a series of three starting liquid compositions (given in Table 5). (Note the significant changes in $\Delta H/\Delta T$ associated with the addition or removal of a phase from the liquidus assemblage compared with the relatively minor changes associated with the replacement of one liquidus phase by another.)

The control of stepwise changes in the enthalpy budget on Θ_{cpp} in fractionating systems

Why does the enthalpy budget affect Θ_{cpp}? We have used microstructural observations to argue that Θ_{cpp} is primarily determined by the rate of plagioclase growth relative to that of augite during the last stages of solidification (and, by extension, Θ_{hpp} is determined by the relative growth rates of plagioclase and orthopyroxene). We suggest that the relative growth rate changes in a stepwise fashion in response to stepwise changes in the temperature derivative of enthalpy.

The addition of a new phase to the liquidus assemblage results in an increase in $\Delta H/\Delta T$. This is manifest by an increase in both the fractional latent heat and the crystal productivity. The former acts to reduce the rate at which the temperature of the intrusion cools. This effect has been observed directly by Dunbar *et al.* (1995), who described a 20 h period of constant temperature that they termed a 'thermal arrest', attributable to the onset of crystallization of the dominant pseudo-cotectic phase assemblage in an $\sim 5\,m^3$ artificial magma body. Although the effects of abrupt changes in fractional latent heat in a larger, and perhaps chemically more complex, natural magma chamber may not be as dramatic (although they might strongly influence the eruption dynamics; Nelson *et al.*, 2011) they will act to slow crystallization and, by analogy with dolerite sills, will change the relative growth rates of plagioclase and augite during the last stages of solidification (see Holness *et al.*, 2012*b*).

The increase of crystal productivity will increase the thickness of the crystal mush on the magma chamber floor, affecting the rates of heat and mass transport through the mush and therefore crystallization rates within the mush. At a given rate of upwards movement of the magma–mush interface, crystallization in the pore spaces of a thicker mush will be slower than that in a thinner mush. The interplay of the effects of changing crystal productivity and fractional latent heat on mush thickness and crystallization rates will depend on the size of the intrusion and the rate at which heat is extracted, but we anticipate that the net effect in kilometre-scale intrusions is to increase the rate of plagioclase growth relative to that of pyroxene, resulting in a stepwise increase in Θ_{cpp}.

That the temperature derivative of enthalpy changes by only a small amount when olivine is replaced by orthopyroxene means that Θ_{cpp} is not affected by such a change of the liquidus assemblage. The loss of olivine without its replacement by orthopyroxene in Sept Iles results in a decrease of fractional latent heat and crystal productivity and a corresponding decrease in the rate of plagioclase growth relative to pyroxene.

CONCLUSIONS

Disequilibrium poly-phase three-grain junctions are ubiquitous in mafic intrusions, and are controlled by processes acting during solidification. The general pattern of spatial variation of the median of these disequilibrium populations of pyroxene–plagioclase–plagioclase dihedral angles is dependent on whether the intrusion is strongly fractionated or not. Non-layered bodies such as sills, in which the liquidus assemblage in the remaining bulk magma was essentially constant throughout solidification, display a symmetric variation of Θ_{cpp} that maps onto the time taken to crystallize in a solidification front of essentially constant composition (Holness *et al.*, 2012*b*). In contrast, Θ_{cpp} in

layered intrusions, in which the cumulus assemblage changes through the stratigraphy in response to effective fractionation, remains constant over large stretches of the stratigraphy, with stepwise changes associated with the addition or subtraction of phases to or from the liquidus assemblage.

The only parameter that behaves in an exactly analogous manner to Θ_{cpp} is the rate of change in enthalpy with temperature $(\Delta H/\Delta T)$ during crystallization. We therefore suggest that the observed variation in Θ_{cpp} is driven by stepwise changes in the temperature derivative of enthalpy that change the cooling and crystallization behaviour of the intrusion, resulting in a stepwise change in the relative rates of growth of plagioclase and pyroxene during the last stages of solidification at the base of the mushy layer. The record of solidification preserved by Θ_{cpp} suggests that the crystallization behaviour of the mushy layer in layered intrusions is thermally buffered through large stretches of the stratigraphy. Microstructures in the Skaergaard UZc suggest that this buffering ceased to operate during the last stages of fractionation.

It is perhaps worth pointing out that the stepwise changes observed in layered intrusions place a maximum bound on the thickness of the crystal mushy layer. The formation of each step requires the thermal regime experienced by the lower parts of the mush layer (where most of the dihedral angles are formed; Holness *et al.*, 2012*b*) to be that relevant to the new liquidus assemblage. That there appears to be precisely the same number of steps as there are changes in the number of phases in liquidus assemblage for each of the four intrusions examined suggests that the mushy layer was nowhere thicker than the stratigraphic distance between the different subdivisions of each intrusion. The shortest of these distances in the intrusions examined here is 300 m (between oxides-in and augite-in of the Sept Iles MCU-I; Fig. 10). Were the mushy layer on the floor of the Sept Iles chamber thicker than 300 m the first of these steps would not have developed.

SUPPLEMENTARY DATA

Supplementary data for this paper are available at *Journal of Petrology* online.

REFERENCES

Bollingberg, K. (1995). Textural and chemical evolution of the Fe–Ti oxide minerals during the late- and post-magmatic cooling of the Skaergaard intrusion, East Greenland. PhD thesis, University of Copenhagen.

Butcher, A. R., Young, I. M. & Faithfull, J. W. (1985). Finger structures in the Rhum Complex. *Geological Magazine* **122**, 491–502.

Cashman, K. V. (1993). Relationship between plagioclase crystallization and cooling rate in basaltic melts. *Contributions to Mineralogy and Petrology* **113**, 126–142.

Cawthorn, R. G. & Walsh, K. L. (1988). The use of phosphorus contents in yielding estimates of the proportion of trapped liquid in cumulates of the Upper Zone of the Bushveld Complex. *Mineralogical Magazine* **52**, 81–89.

Charlier, B., Namur, O. & Grove, T. L. (2013). Compositional and kinetic controls on liquid immiscibility in ferrobasalt–rhyolite volcanic and plutonic series. *Geochimica et Cosmochimica Acta* **113**, 79–93.

Cimon, J. (1998). *Le Complexe de Sept-Îles: I—L'Unité à apatite de Rivière des Rapides, Complexe de Sept-Îles; localisation stratigraphique et facteurs à l'origine de sa formation.* Québec: Ministère de l'Energie et des Ressources du Québec, pp. 1–33.

Dunbar, N. W., Jacobs, G. K. & Naney, M. T. (1995). Crystallisation processes in an artificial magma: variations in crystal shape, growth rate and composition with melt cooling history. *Contributions to Mineralogy and Petrology* **120**, 412–425.

Emeleus, C. H. (1997). *Geology of Rum and the Adjacent Islands. Memoir of the British Geological Survey, Sheet 60 (Scotland).* Keyworth, Nottingham: British Geological Survey.

Emeleus, C. H., Cheadle, M. J., Hunter, R. H., Upton, B. G. J. & Wadsworth, W. J. (1996). The Rum Layered Suite. In: Cawthorn, R. G. (ed.) *Layered Intrusions. Developments in Petrology* **15**, 403–440.

Ghiorso, M. S. (1997). Thermodynamic models of igneous processes. *Annual Review of Earth and Planetary Sciences* **25**, 221–241.

Ghiorso, M. S. & Sack, R. O. (1995). Chemical mass transfer in magmatic processes. IV. A revised and internally consistent thermodynamic model for the interpolation and extrapolation of liquid–solid equilibria in magmatic systems at elevated temperatures and pressures. *Contributions to Mineralogy and Petrology* **119**, 197–212.

Ghiorso, M. S., Hirschmann, M. M., Reiners, P. W. & Kress, V. C. (2002). The pMELTS: An revision of MELTS aimed at improving calculation of phase relations and major element partitioning involved in partial melting of the mantle at pressures up to 3 GPa. *Geochemistry, Geophysics, Geosystems* **3**, doi:10.1029/2001GC000217.

Gleason, G. C., Bruce, V. & Green, H. W. (1999). Experimental investigation of melt topology in partially molten quartzofeldspatic aggregates under hydrostatic and nonhydrostatic stress. *Journal of Metamorphic Geology* **17**, 705–722.

Helz, R. T. (1987). Differentiation behavior of Kilauea Iki lava lake, Kilauea volcano, Hawaii: An overview of past and current work. In: Mysen, B. O. (ed.) *Magmatic Processes: Physicochemical Principles. Geochemical Society Special Publication* **1**, 241–258.

Higgins, M. D. (2005). A new model for the structure of the Sept Iles Intrusive suite, Canada. *Lithos* **83**, 199–213.

Higgins, M. D. & van Breeman, O. (1998). The age of the Sept Iles layered mafic intrusion, Canada: Implications for the Late Neoproterozoic/Cambrian history of Southeastern Canada. *Journal of Geology* **106**, 421–431.

Holness, M. B. (2007). Textural immaturity of cumulates as an indicator of magma chamber processes: infiltration and crystal accumulation in the Rum Layered Suite. *Journal of the Geological Society, London* **164**, 529–539.

Holness, M. B. (2010). Decoding dihedral angles in melt-bearing and solidified rocks. In: Forster, M. A., Fitz Gerald, J. D. & Lister, G. S. (eds) *Journal of the Virtual Explorer* **35**, paper 3, doi:10.3809/jvirtex.2010.00265.

Holness, M. B. & Humphreys, M. C. S. (2003). The Traigh Bhàn na Sgùrra sill, Isle of Mull: flow localization in a major magma conduit. *Journal of Petrology* **44**, 1961–1976.

Holness, M. B. & Winpenny, B. (2009). The Unit 12 allivalite, Eastern Layered Intrusion, Isle of Rum: a textural and geochemical study of an open-system magma chamber. *Geological Magazine* **146**, 437–450.

Holness, M. B., Cheadle, M. J. & McKenzie, D. (2005). On the use of changes in dihedral angle to decode late-stage textural evolution in cumulates. *Journal of Petrology* **46**, 1565–1583.

Holness, M. B., Nielsen, T. F. D. & Tegner, C. (2007a). Textural maturity of cumulates: a record of chamber filling, liquidus assemblage, cooling rate and large-scale convection in mafic layered intrusions. *Journal of Petrology* **48**, 141–157.

Holness, M. B., Tegner, C., Nielsen, T. F. N., Stripp, G. R. & Morse, S. A. (2007b). A textural record of solidification and cooling in the Skaergaard intrusion, East Greenland. *Journal of Petrology* **48**, 2359–2377.

Holness, M. B., Hallworth, M. A., Woods, A. & Sides, R. E. (2007c). Infiltration metasomatism of cumulates by intrusive magma replenishment: the Wavy Horizon, Isle of Rum, Scotland. *Journal of Petrology* **48**, 563–587.

Holness, M. B., Morse, S. A. & Tegner, C. (2009). Response to comment by McBirney, Boudreau and Marsh. *Journal of Petrology* **50**, 97–102.

Holness, M. B., Stripp, G., Humphreys, M. C. S., Veksler, I. V., Nielsen, T. F. D. & Tegner, C. (2011). Silicate liquid immiscibility within the crystal mush: late-stage magmatic microstructures in the Skaergaard intrusion, East Greenland. *Journal of Petrology* **52**, 175–222.

Holness, M. B., Humphreys, M. C. S., Sides, R., Helz, R. T. & Tegner, C. (2012a). Towards an understanding of disequilibrium dihedral angles in mafic rocks. *Journal of Geophysical Research*, doi:10.1029/2011JB008902.

Holness, M. B., Richardson, C. & Helz, R. T. (2012b). Disequilibrium dihedral angles in dolerite sills: a new proxy for cooling rate. *Geology* **40**, 795–798.

Hoover, J. D. (1989). Petrology of the Marginal Border Series of the Skaergaard intrusion. *Journal of Petrology* **30**, 399–439.

Huppert, H. E. & Turner, J. S. (1991). Comments on 'On convective style and vigor in sheet-like magma chambers' by Bruce D. Marsh. *Journal of Petrology* **32**, 851–854.

Irvine, T. N. (1982). Terminology for layered intrusions. *Journal of Petrology* **23**, 127–162.

Irvine, T. N., Andersen, J. C. & Brooks, C. K. (1998). Included blocks (and blocks within blocks) in the Skaergaard intrusion: geological relations and the origins of rhythmic modally graded layers. *Geological Society of America Bulletin* **110**, 1398–1447.

Kruger, F. J., Cawthorn, R. G. & Walsh, K. L. (1987). Strontium isotopic evidence against magma addition in the Upper Zone of the Bushveld Complex. *Earth and Planetary Science Letters* **84**, 51–58.

Latypov, R. (2009). Testing the validity of the petrological hypothesis 'no phenocrysts, no post-emplacement differentiation'. *Journal of Petrology* **50**, 1047–1069.

Libourel, G., Boivin, P. & Biggar, G. M. (1989). The univariant curve liquid = forsterite + anorthite + diopside in the system CMAS at 1 bar: solid solutions and melt structure. *Contributions to Mineralogy and Petrology* **102**, 406–421.

Longhi, J. (1987). Liquidus equilibria and solid solution in the system Anorthite–Forsterite–Wollastonite–Silica at low pressure. *American Journal of Science* **287**, 265–331.

Marsh, B. D. (1989). On convective style and vigor in sheet-like magma chambers. *Journal of Petrology* **30**, 479–530.

Marsh, B. D. (1991). Reply to comments. *Journal of Petrology* **32**, 855–860.

Marsh, B. D. (2006). Dynamics of magmatic systems. *Elements* **2**, 287–292.

McBirney, A. R., Boudreau, A. E. & Marsh, B. D. (2009). Comments on: 'Textural maturity of cumulates: a record of chamber filling, liquidus assemblage, cooling rate and large-scale convection in mafic layered intrusions' and 'A textural record of solidification and cooling in the Skaergaard intrusion, East Greenland'. *Journal of Petrology* **50**, 93–95.

McKenzie, D. (2011). Compaction and crystallization in magma chambers: towards a model of the Skaergaard intrusion. *Journal of Petrology* **52**, 905–930.

Molyneux, T. G. (1974). A geological investigation of the Bushveld Complex in Sekhukhuneland and part of the Steelport valley. *Transactions of the Geological Society of South Africa* **77**, 329–338.

Morse, S. A. (1986). Convection in aid of adcumulus growth. *Journal of Petrology* **27**, 1183–1214.

Morse, S. A. (2011). The fractional latent heat of crystallizing magmas. *American Mineralogist* **96**, 682–689.

Morse, S. A., Owen, B. E. & Butcher, A. R. (1987). Origin of finger structures in the Rhum Complex: phase equilibrium and heat effects. *Geological Magazine* **124**, 205–210.

Namur, O. & Charlier, B. (2012). Efficiency of compaction and compositional convection during mafic crystal mush solidification: The Sept Iles layered intrusion, Canada. *Contributions to Mineralogy and Petrology* **163**, 1069–1082.

Namur, O., Charlier, B., Toplis, M. J., Higgins, M. D., Liégeois, J.-P. & Vander Auwera, J. (2010). Crystallisation sequence and magma chamber processes in the ferrobasaltic Sept Iles layered intrusion, Canada. *Journal of Petrology* **51**, 1203–1236.

Namur, O., Charlier, B., Toplis, M. J., Higgins, M. D., Hounsell, V., Liégeois, J. P. & Vander Auwera, J. (2011). Differentiation of tholeiitic basalt to A-type granite in the Sept Iles layered intrusion, Canada. *Journal of Petrology* **52**, 487–539.

Namur, O., Charlier, B. & Holness, M. (2012). Dual origin of Fe–Ti–P gabbros by immiscibility and fractional crystallization of evolved tholeiitic basalts in the Sept Iles layered intrusion. *Lithos* **154**, 100–114.

Naslund, H. R. (1984). Petrology of the Upper Border Series of the Skaergaard intrusion. *Journal of Petrology* **25**, 185–212.

Nelson, B. K., Ghiorso, M. S., Bachmann, O. & Dufek, J. (2011). Modeling the Daly Gap: the influence of latent heat production in controlling magma extraction and eruption, American Geophysical Union, Fall Meeting 2011, Abstract V43A-2563.

Nielsen, T. F. D. (2004). The shape and volume of the Skaergaard Intrusion, East Greenland: Implications for mass balance and bulk composition. *Journal of Petrology* **45**, 507–530.

Philpotts, A. R., Shi, J. & Brustman, C. (1998). Role of plagioclase crystal chains in the differentiation of partly crystallized basaltic magma. *Nature* **395**, 343–346.

Philpotts, A. R., Brustman, C. M., Shi, J., Carlson, W. D. & Denison, C. (1999). Plagioclase-chain networks in slowly cooled basaltic magma. *American Mineralogist* **84**, 1819–1829.

Presnall, D. C., Dixon, J. R., O'Donnell, T. H. & Dixon, S. A. (1979). Generation of mid-ocean ridge tholeiites. *Journal of Petrology* **20**, 3–35.

Renner, R. & Palacz, Z. (1987). Basaltic replenishment of the Rhum magma chamber: evidence from unit 14. *Journal of the Geological Society, London* **144**, 961–970.

Riegger, O. K. & van Vlack, L. H. (1960). Dihedral angle measurements. *Transactions of the Metallurgical Society of the AIME* **218**, 933–935.

Salmonsen, L. P. & Tegner, C. (2013). Crystallisation sequence of the Upper Border Series of the Skaergaard Intrusion: revised subdivision and implications for chamber-scale magma homogeneity. *Contributions to Mineralogy and Petrology* **165**, 1155–1171.

Shi, P. & Libourel, G. (1991). The effects of FeO on the system CMAS at low pressure and implications for basalt crystallization processes. *Contributions to Mineralogy and Petrology* **108**, 129–145.

Sides, R. (2008). Crystal mushes in mafic magma chambers. PhD thesis, University of Cambridge.

Stickels, C. A. & Hücke, E. E. (1964). Measurement of dihedral angles. *Transactions of the Metallurgical Society of the AIME* **230**, 795–801.

Tait, S. R. (1985). Fluid dynamic and geochemical evolution of cyclic unit 10, Rhum, Eastern Layered Series. *Geological Magazine* **122**, 469–484.

Tait, S. & Jaupart, C. (1992). Compositional convection in a reactive crystalline mush and melt differentiation. *Journal of Geophysical Research* **97**, 6735–6756.

Tegner, C. & Cawthorn, R. G. (2010). Iron in plagioclase in the Bushveld and Skaergaard intrusions: implications for iron contents in evolving basic magmas. *Contributions to Mineralogy and Petrology* **159**, 719–730.

Tegner, C., Cawthorn, R. G. & Kruger, F. J. (2006). Cyclicity in the Main and Upper Zones of the Bushveld complex, South Africa: crystallization from a zoned magma sheet. *Journal of Petrology* **47**, 2257–2279.

Tegner, C., Thy, P., Holness, M. B., Jakobsen, J. K. & Lesher, C. (2009). Differentiation and compaction in the Skaergaard intrusion. *Journal of Petrology* **50**, 813–840.

Thy, P., Lesher, C. E., Nielsen, T. F. D. & Brooks, C. K. (2006). Experimental constraints on the Skaergaard liquid line of descent. *Lithos* **92**, 154–180.

Toplis, M. J. & Carroll, M. R. (1995). An experimental study of the influence of oxygen fugacity on Fe–Ti oxide stability, phase relations, and mineral–melt equilibria in ferro-basaltic systems. *Journal of Petrology* **36**, 1137–1170.

Toplis, M. J., Libourel, G. & Carroll, M. R. (1994). The role of phosphorus in crystallization processes of basalt: an experimental study. *Geochimica et Cosmochimica Acta* **58**, 797–810.

Vernon, R. H. (1968). Microstructures of high-grade metamorphic rocks at Broken Hill, Australia. *Journal of Petrology* **9**, 1–22.

Voll, G. (1960). New work on petrofabrics. *Liverpool and Manchester Geological Journal* **2**, 503–567.

von Gruenewaldt, G. (1970). On the phase change orthopyroxene–pigeonite and the resulting textures in the Main and Upper Zones of the Bushveld Complex in the eastern Transvaal. In: Visser, D. J. L. & von Gruenewaldt, G. (eds) *Symposium on the Bushveld Igneous Complex and Other Layered Intrusions.* Johannesburg: Geological Society of South Africa, pp. 67–73.

von Gruenewaldt, G. (1973). The main and upper zones of the Bushveld Complex in the Roossenekal area, Eastern Transvaal. *Geological Society of South Africa Transactions* **76**, 207–227.

Wager, L. R. & Brown, G. M. (1968). *Layered Igneous Rocks*. London: Oliver & Boyd, 572 p.

Wager, L. R. & Deer, W. A. (1939). Geological investigations in East Greenland. Pt III. The petrology of the Skaergaard intrusion. Kangerdlugssuaq, East Greenland. *Meddeleser om Grønland* **105**, 1–352.